Advances in Erbium-Doped Nanostructures: From Nanothermometry Applications to Single Photon Emission and Microresonator Innovations

by

Elham HOSSEINI TOODESHKI

M.Sc., University of Tehran, 2016

B.Sc., Sharif University of Technology, 2014

A dissertation submitted in partial fulfillment of the requirements

for the degree of

Doctor of Philosophy

Department of Electrical and Computer Engineering

University of Victoria

Advances in Erbium-Doped Nanostructures: From Nanothermometry Applications to Single Photon Emission and Microresonator Innovations

by

Elham HOSSEINI TOODESHKI

M.Sc., University of Tehran, 2016

B.Sc., Sharif University of Technology, 2014

Supervisory Committee

Dr. Reuven GORDON, **Supervisor**

Department of Electrical and Computer Engineering

Dr. Jens BORNEMANN, **Committee Member**

Department of Electrical and Computer Engineering

Dr. Andrew MACRAE, **Committee Member**

Department of Physics and Astronomy

Abstract

This dissertation examines erbium-doped micro and nanostructures in-depth, with a focus on optical properties and fabrication techniques. It investigates nanothermometry, emphasizing the stoichiometric control possible in these materials, and demonstrates ratiometric temperature measurement at the nanoscale. The research achieves significant results in trapping erbium-containing nanocrystals using optical tweezers and nanoaperture trapping techniques, establishing their capabilities as single-photon sources. The study goes on to describe the fabrication of erbium-doped silica microcavities and thin films using the sol-gel method, revealing their potential in creating microdisks that support low-threshold lasing.

Table of Contents

List of Figures

Acknowledgements

I would like to thank my supervisor, Dr. Reuven Gordon, for his invaluable support and insight throughout my studies. I am deeply grateful to my collaborators and colleagues in the Nanoplasmonics Research Group for their support and encouragement, including Michael Dobinson, Mirali Seyed Shariatdoust, Ghazal Hajisalem, Demelza Wright, Elham Babaei, Behnam Khosravi, and Matthew Peters. Additionally, I appreciate the collaboration with Dr. Frank C.J.M. van Veggel and Adriaan Frencken from the Department of Chemistry. I want to express my deepest appreciation to my dear partner, family, and friends for their unwavering motivation, love, and support. Lastly, I would like to acknowledge the assistance ChatGPT provided while writing my thesis. The use of this AI model helped me generate content and explore different ideas. However, it is important to note that all information generated by ChatGPT was thoroughly reviewed and revised by this author to ensure its accuracy and appropriateness for my dissertation.

Glossary

APD	**A**valanche **P**hoto**d**iode
CCD	**C**harge-**c**oupled **D**evice
CMOS	**C**omplementary **m**etal–**o**xide–**s**emiconductor
CW	**C**ontinuous **W**ave
DAQ	**D**ata **Ac****q**uisition
DNH	**D**ouble **N**ano**h**ole
EDFA	**E**rbium-**D**oped **F**iber **A**mplifier
HBT	**H**anbury-**B**rown-**T**wiss
HOM	**H**ong-**O**u-**M**andel
HWP	**H**alf-**w**ave **P**late
IR	**I**nfra**r**ed
LP	**L**inear **P**olarizer
LPF	**L**ong-**p**ass **F**ilter
MMF	**M**ulti-**m**ode Optical **F**iber
NA	**N**umerical **A**perture
NAFT	**N**ano**a**perture Optical **F**iber **T**weezers
NIR	**N**ear-**i**nfra**r**ed
NP	**N**ano**p**article
pHP	***p*-h**ydroxy**p**henacyl
PVC	**P**oly**v**inyl **C**hloride
RMS	**R**oot **M**ean **S**quare
SEM	**S**canning **E**lectron **M**icroscope
SPF	**S**hort-**p**ass **F**ilter
SMF	**S**ingle-**m**ode Optical **F**iber
SNSPD	**S**uper-conducting **N**anowire **S**ingle **P**hoton **D**etector
UV	**U**ltra**v**iolet

List of Symbols

Symbol	Name	Unit
α	polarizability	$\mathrm{C\,m^2\,V^{-1}}$
α_c	attenuation	$\mathrm{dB\,km^{-1}}$
β	propagation constant	$\mathrm{rad\,m^{-1}}$
γ	decay rate	$\mathrm{s^{-1}}$
ε_0	vacuum permittivity	$\mathrm{F\,m^{-1}}$
ε_r	relative permittivity	(1)
η	quantum efficiency	(1)
λ	wavelength	m
μ_0	vacuum permeability	$\mathrm{H\,m^{-1}}$
μ_r	relative permeability	(1)
τ	time delay	s
ω	angular frequency	$\mathrm{rad\,s^{-1}}$
$\mathcal{C}$	counts	(1)
k	wavenumber	$\mathrm{m^{-1}}$
n	refractive index	(1)
P	power	W ($\mathrm{J\,s^{-1}}$)
Q	quality factor	(1)
t	time	s
T	transmission	(1)
r	radius	m
V	volume	$\mathrm{m^3}$
$\mathbf{E}$	electric field vector	$\mathrm{V\,m^{-1}}$
$\mathbf{p}$	dipole moment vector	C m
$\mathbf{r}$	position vector	m
∇	vector differential operator	–
$\langle\,\rangle$	time average	–
$\perp$	perpendicular	–
$\parallel$	parallel	–

Chapter 1

Introduction

The primary objective of this dissertation is to investigate the optical properties of erbium (Er) doped micro and nanostructures. The research encompasses the measurement and study of various optical properties of these structures, along with a focus on the methods for fabricating Er-doped silica thin films, microresonators, and nanoapertures for immobilizing Er-doped nanocrystals.

Erbium is applicable in many technologies because of its unique properties. Shahrjerdi et al. used Er as a contact material in carbon nanotube (CNT) transistors to improve their performance and stability. This research found that Er contacts enhanced electron injection and transport, resulting in higher electron mobility and better device performance. Also, the Er contacts improved the stability of the CNT transistors, which is an important factor for practical device applications [1]. Solar energy conversion is another application of Er. Upconversion is a phenomenon whereby photons of lower energy are transformed into photons of higher energy, which can then be used to generate electricity in solar cells. Compared to other upconverting materials, Er has high upconversion efficiency and compatibility with

silicon solar cells, which makes it a good candidate for energy conversion [2]. Researchers have studied the application of lanthanide-doped upconversion materials, including Er, for improving the Collection of light and movement of electrical charges within organic photovoltaic devices. Fei Wang et al. synthesized Er-doped upconverting nanoparticles (UCNPs) and incorporated them into organic solar cells. They found that the UCNPs improved the light harvesting efficiency of the solar cells and enhanced charge transport, resulting in higher device efficiency. Er-doped UCNPs exhibited higher upconversion efficiency than other lanthanide-doped UCNPs [3]. Er-doped nanocrystals can be a potentially stable source of single photons at the 1550 nm wavelength. Researchers could isolate individual Er ions in nanocrystals and demonstrate their ability to emit single photons. The use of Er as a single-photon source has advantages over other materials, such as quantum dots, which can be difficult to stabilize and control [4], [5]. Er-doped optical fibers can be used for quantum storage of entangled photons at the telecom wavelength. The researchers were able to store entangled photons in the Er-doped fiber for up to 100 microseconds, which is long enough for many quantum communication protocols [6].

Erbium is used in nanothermometry as a luminescent temperature probe. When Er ions are embedded in a nanostructure, they emit light at specific wavelengths when excited by an external light source. The change of intensity ratio of these

emissions is a measure of temperature change, allowing Er to be used as a temperature sensor. In nanothermometry, Er-doped nanoparticles are used as nanothermometers [7]. These nanoparticles are very small, typically less than 100 nm in diameter, and can be embedded in a material or placed in a biological sample. By measuring the intensity of the Er luminescence, the temperature of the surrounding environment can be determined with high precision. Er-based nanothermometry has many potential applications, including in nanoelectronics, biomedicine, and materials science. It offers several advantages over other temperature-sensing methods, such as high sensitivity, small size, and compatibility with a wide range of materials and environments.

Erbium is widely used in the field of microresonators, and significant advances have been made in this field. Microresonators, such as silicon photonics-based devices, have made significant progress in a variety of applications, including on-chip light sources and optical communication systems [8]–[10]. The high quality factor (Q) of microresonator modes, which results in narrow resonance linewidths and high optical intensities, is critical for accommodating multiple wavelength-division multiplexing (WDM) channels within the communication window of Er amplifiers [9]. Furthermore, the use of Er in microresonators has broadened the application fields, allowing for tunable luminescence colours and self-reference biosensing [11]. This collective progress emphasizes the significance of Er in the advancement of microresonator technologies in a variety of domains. Berneschi et al.

investigated micro-laser sources in Er-doped microcavities and their potential applications in filtering, optical switching, and sensing in a study on glass-based microresonators. They emphasized these microresonators' exceptional performance, attributing it to their high surface quality and ability to enhance functionalities through coatings [12]. In a related study, Rasoloniaina et al. demonstrated the ability to control coupling properties in active ultrahigh-Q whispering gallery mode (WGM) microcavities by adjusting the pumping rate, emphasizing the role of Er ions in compensating for losses and achieving spectral selective amplification. This work paves the way for future research in nonlinear optics with low thresholds and integrated optical sensors. [13]. In addition, Liu et al. incorporated Er into a photonic integrated circuit-based amplifier, taking advantage of its ability to amplify optical signals within ultralow-loss silicon nitride waveguides. This implementation, which mimics the amplification process in traditional Er-doped fiber amplifiers, represents a significant advancement in telecommunications and optical sensing applications because it significantly increases the output power of soliton microcombs, aligning with the power requirements of various critical applications like the generation of microwave signals using photonics and optical communications with multiple wavelengths, known as wavelength-division multiplexing. These studies highlight the critical role of Er in the advancement of microresonator technologies, as well as its potential for driving innovation in a wide range of practical applications, from optical communication systems to integrated optical sensors and photonic circuits [14].

1.1 Erbium in Nanostructures

1.1.1 Nanothermometry

Nanothermometry refers to the measurement of temperature at the nanoscale, typically using nanoscale materials as temperature sensors. This field has received growing attention in recent years because of the increasing demand for high-resolution thermal measurements in various applications, such as in nanoelectronics, energy storage, and biomedicine. One common approach to nanoscale temperature measurement is to use nanoscale particles or structures that exhibit temperature-dependent optical or magnetic properties. For example, semiconductor nanocrystals, also known as quantum dots, can emit light with intensity that depends on their temperature, and this property can be used to infer the local temperature. Similarly, magnetic nanoparticles can exhibit temperature-dependent magnetic relaxation times, which can be used to measure temperature [15], [16].

Ratiometric thermometry using Er emission is an advanced technique in temperature sensing that leverages the unique luminescent properties of Er-doped materials [17]. In ratiometric analysis, the temperature is determined by measuring the ratio of luminescence intensities at two unlike wavelengths, rather than the absolute intensity of a single emission peak [18]. This approach compensates for potential fluctuations in the excitation source or the sensor's environment, offering

enhanced accuracy and stability. The principle of ratiometric thermometry typically involves monitoring the emission intensities from two thermally coupled levels of the Er ion. As the temperature changes, the population of ions in these levels adjusts according to Boltzmann distribution, leading to a temperature-dependent variation in the intensity ratio of the emitted light. This method is especially valuable as it inherently corrects for common sensing errors like fluctuations in excitation power or optical path losses [19]. Novel approaches for temperature sensing and information security were presented by utilizing the ultrahigh thermoresponsive upconversion of Er ions embedded in a nanomaterial. The fluorescence intensity ratio of the Er ions is sensitive to temperature changes, enabling accurate temperature measurements with a high resolution of 0.2 K [20].

1.1.2 Single Photon Emission

Erbium ions in silicon represent a promising avenue for advancing quantum technologies, particularly because of their potential to emit single photons, which are crucial for quantum communication, cryptography, and computing. However, the efficiency of single-photon emitters using Er ions in silicon is constrained. This is primarily because of the low emission probability of Er ions and the challenges in efficiently coupling the emitted photons with the external environment [21]. To enhance the performance of these single-photon emitters, researchers have designed Er-doped silicon nanocavities. These structures effectively confine light in a

small volume, increasing the interaction between photons and emitters [21]. Optical tweezers, which manipulate particles through the momentum changes caused by light scattering and absorption, also play a vital role. The phenomenon of light scattering is particularly relevant when a particle approaches a laser's focal point, leading to a shift in momentum and causing the particle to move toward the focus [22]. Despite extensive research on single-photon sources, a high-quality, accessible, and cost-effective source suitable for mass production remains elusive [23]. An individual photon emitter operating at the 1550 nm telecommunication wavelength is crucial for expansive quantum communication networks due to this wavelength's minimal signal loss in fiber-optic systems [24]. Various candidates exist for single-photon sources, including individual ions [25], atoms, molecules, quantum dots, colour centers, and atomic ensembles. Among these, single-photon sources based on Er ions are notable for their emission in the low-loss fibre optic telecommunication wavelengths and extended coherence durations. However, the challenges with Er emitters include their lower brightness compared to other sources and the difficulty in isolating single emitters in a scalable manner [4]. A quantum emitter capable of emitting one photon at a time is classified as a single-photon source. Creating single-photon sources that are luminous, fast, and manageable presents a substantial hurdle in the field of quantum information and communication. Typically, in a uniform setting, these single-photon emitters face issues like diminished luminosity, extended fluorescence lifetimes, and inefficient photon gathering [5].

Er-doped nanocrystals, which can be pumped using inexpensive lasers and emit light at telecommunication wavelengths, are ideal for fiber optic network transmission. Isolating a single nanocrystal containing an active Er emitter is crucial for creating single-photon sources [26]. Optical trapping, which enables the isolation of single particles, is used to assess their potential as quantum light sources. In conjunction with optical trapping, metallic nanostructures can enhance the incident field and optical forces, facilitating the evaluation of particles as small as 100 nm [27]. By optically trapping single Er-doped nanocrystals and stimulating them using plasmon-enhanced double nanohole (DNH) apertures, their optical properties can be examined.

Furthermore, a photochemical approach for permanently anchoring nanocrystals inside a DNH aperture while optically trapped was explored [28]. This method, combining emission enhancement and isolation of Er-doped nanocrystals, may lead to a strategy for anchoring nanocrystals with single active emitters permanently. Such a device, operable at cryogenic temperatures, could generate single photons on demand and couple them to an optical fibre for quantum communication.

1.2 Erbium in Microstructures

There have been significant advancements made in a variety of forms of microresonators, which are used in a wide variety of applications. Particularly, microspheres and microdisks have gained prominence as key types of microresonators, due to their roles in applications that require ultra-narrow linewidths, leverage cavity Quantum Electrodynamics (QED) principles, and utilize microlasers with exceedingly low activation thresholds. A tangential light injection is utilized by these resonators, which include the Whispering Gallery Mode (WGM) types that are composed of microspheres and circular cavities. This phenomenon results in light being confined in circular paths immediately beneath the surface, maintained by continuous total internal reflections. This results in a high Q due to the fact that the confinement mechanism experiences minimal dissipation [29]–[32]. Microresonators have found extensive use in fields like nonlinear optics, quantum electrodynamics, and bio-molecule sensing [33], [34]. An emerging area of interest lies in exploring new materials for application in low-threshold microlasers. WGM microresonators are compact optical devices that are used in a variety of applications including sensing, filtering, and optical signal processing. Erbium is an essential component in the mechanism that allows these microresonators to function properly. By utilizing the principle of total internal reflection, these microresonators can capture light within their circular or spherical cavities, which results in the generation of optical resonances of superior quality [29], [35], [36].

Er-doped WGM microresonators are highly effective as sensitive and selective

sensors. They are used in a variety of applications, including temperature and pressure sensing, as well as the detection of volatile organic compounds (VOCs). Erbium doping enhances the coupling between the resonator and its environment, which leads to increased sensitivity in detection [35], [37]. In optical communication, Er-doped WGM microresonators play a significant role, particularly in WDM systems. By adjusting the diameter of the microresonator, the resonant wavelengths can be tuned to align with specific channels in WDM systems. This feature enables the simultaneous transmission of multiple signals through a single optical fiber [29], [38]. Nonlinear optical phenomena like Stimulated Raman Scattering (SRS) and the inversion of population levels in rare earth ions within a host material are both capable of generating optical gain [39]. For low-threshold microlasers, microcavities with a high degree of delicacy make suitable candidates. Researchers later discovered SRS from CS_2 microdroplets [40]. Cai [41] has developed Nd-doped silica microsphere and Er-doped phosphate microsphere microlasers. The focus of this project was the direct processing of Er-doped silica films using the sol-gel technique to create microdisks applicable for low-threshold lasing.

1.3 Contributions

The study of nanothermometry has garnered significant attention in recent years because of its potential applications in various fields, including biomedicine, materials science, and nanotechnology. One promising approach for nanothermometry involves using Er-doped nanocrystals, which can emit visible and near-infrared

light when excited by a suitable energy source. In this research, we focus on three aspects of nanothermometry using Er-doped nanocrystals: (1) developing a reliable method for temperature sensing using these particles, (2) attaching them to an optical tweezer for precise control and manipulation, and (3) investigating the green emission from Er-doped silica microcavities.

Firstly, our research aims to develop a reliable method for temperature sensing using Er-doped nanocrystals isolated using an optical tweezer. Optical tweezers use a focused laser beam to trap and manipulate small particles, enabling precise control over their position and orientation. Erbium ions have been shown to exhibit strong temperature dependence in their optical properties, making them ideal candidates for nanothermometry applications. We aim to develop a robust and accurate nanothermometry platform using Er-doped nanocrystals.

Secondly, we are investigating the use of optical tweezers for attaching Er-doped nanocrystals to specific locations for precise temperature sensing or as a single photon source. By attaching Er-doped nanocrystals to an optical tweezer, we can achieve high spatial resolution in temperature measurements, which are particularly useful in complex environments such as living cells or tissue.

Lastly, we are investigating the green emission from Er-doped silica microcavities, presenting a promising avenue for the development of innovative devices. These microcavities function as optical resonators, confining light in a diminutive volume, which in turn magnifies the interaction between light and the Er ions. The embedded Er ions are capable of emitting green light upon laser excitation, with

the intensity of this emission being acutely sensitive to the microcavity's ambient temperature. This characteristic sensitivity to temperature variations positions Er-doped silica microcavities as potential candidates for high-resolution, sensitive nanothermometry applications. Furthermore, the unique properties of these microcavities hold great promise not only for temperature sensing but also for the creation of single-photon sources and low-threshold lasers, thereby opening up new frontiers in quantum communication and sensing technologies.

In summary, our research contributes to the development of a reliable and accurate nanothermometry platform using Er-doped nanocrystals. We investigate using optical tweezers for precise control and manipulation of these particles and explore the green emission from Er-doped silica microcavities for additional capabilities. Our findings can have significant implications for various fields, including biomedicine, materials science, and nanotechnology.

Microstructure Contribution

In the study on Er-doped silica microdisk resonators, Elham Hosseini Toodeshki performed all the research steps. The work focused on optimizing the fabrication process to achieve high-quality thin films and structurally sound microdisks. This involved meticulously controlling the sol-gel synthesis and annealing steps to ensure the uniformity and crack-free nature of the silica thin films. The microdisks were then fabricated using a combination of deep UV photolithography, HF wet etch, and XeF_2 dry etch, carefully monitored to achieve the desired microdisk shape

and size. One of the critical aspects of this contribution was addressing the challenge of minimizing structural weaknesses and cracks in the thin films, which directly impact the Q factor of the microdisks. By refining the etching protocols and optimizing the fabrication parameters, the author was able to produce microdisks with high intrinsic Q factors, indicative of their efficiency in light confinement and minimal energy loss. These advancements not only demonstrate technical proficiency but also pave the way for enhanced performance in applications such as optical sensing, telecommunications, and photonics.

The dissertation discusses three published works to which the author contributed, together with other investigative work not yet disclosed in a published journal. The contributions of the author in each published work are detailed as follows:

Thermometric Analysis of Nanoaperture Trapped Erbium Containing Nanocrystals

Elham Hosseini Toodeshki carried out all the nanofabrication processes, performed measurements and analyses, and was also in charge of the manuscript composition. Adriaan Frencken and Frank C.J.M. van Veggel synthesized the utilized nanocrystals. Reuven Gordon conceptualized the experiments, offered advice on data analysis, and contributed to writing the manuscript.

Photochemical Anchoring of Singly Er^{3+} Ion-Doped $NaYF_4$ Nanoparticles for Scalable Fabrication of Single-Photon Emitting Devices: Implications for Quantum Light Sources in the Telecom Window

Adriaan Frencken synthesized and modified the nanocrystals and wrote the

manuscript. Michael Dobinson performed the nanofabrication processes, primary measurements, and characterization. Zohreh Sharifi assisted in the creation of the figures. Elham Hosseini Toodeshki performed additional trapping experiments and provided figures. Frank C.J.M. van Veggel and Reuven Gordon designed the experiments and offered expert advice and direction in interpreting and analyzing the experimental data.

Nanoscale upconverter thermometers in a double-nanohole optical tweezer

Elham Hosseini Toodeshki conducted all the nanofabrication processes, performed the measurements and analyses, and took the lead in composing the manuscript. The nanocrystals used in the study were synthesized by Adriaan Frencken and Frank C.J.M. van Veggel. Reuven Gordon conceptualized the experiments, provided guidance on data analysis, and assisted in writing the manuscript.

Chapter 2

Theory

In this chapter, we investigate several key technologies crucial to the advancement of quantum science. Our focus encompasses the mechanics and applications of optical tweezers, nanoapertures, and the innovative field of nanothermometry. We explore the operation and enhancement of optical tweezers, particularly through the integration of nanoaperture technology for nanoscale particle manipulation. Attention is given to the precise measurement of temperature at the nanoscale, emphasizing the fluorescence intensity ratio method and the importance of upconverting nanoparticles in accurate temperature assessment. Additionally, the chapter examines the fabrication and significance of Er-doped silica microresonators, underscoring their contribution to the development of single-photon sources for quantum technologies.

2.1 Optical Tweezers

Optical tweezers utilize optical forces, typically generated by a laser, to maintain the position of particles. Traditional optical tweezers, which employ a single focused beam, are effective in trapping dielectric particles larger than 100 nm in size, operating in the Rayleigh and Mie regime. This method avoids the need for intense optical power that could potentially damage the particles [42]. With low optical powers, nanoaperture optical tweezers may explore far smaller particles, enabling single proteins in the nanometer range to be caught without damage [27]. The gradient force generated by a focussed laser on a particle with a different refractive index than the surrounding medium is employed in optical trapping.

Ashkin and colleagues pioneered the exploration of this phenomenon, establishing it as a widely adopted method for capturing and manipulating nanoparticles. The process utilizes a focused beam that generates a gradient force, F_{grad}, serving as a restorative force to maintain the particle within the beam's most intense zone. This gradient force is counterbalanced by the scattering force, F_{scat}, ensuring the particle remains within the optical trap. This technique is particularly effective for nanoparticles in the Mie regime, where their size exceeds the incoming light's wavelength. However, when particle sizes fall into the smaller Rayleigh domain, marked by $2r < 0.2\lambda$, they still can be trapped using a single focused beam, but at the cost of requiring extremely high intensities. These high intensities often lead to significant heating and potential damage to the particles. This effect is due to Rayleigh scattering, which exerts a force in the direction of the incident

power, scaling with the particle's radius to the sixth power (r^6). To keep the particle captured, the scattering force should be matched with the gradient force. For smaller nanoparticles, maintaining the optical trap is challenging as the gradient force increases with the cube of the radius, r^3. In such cases, the gradient force is influenced by the electric field gradient $\nabla \mathbf{E}$, as well as the refractive indices of the medium n_m and the particle n_p [42]:

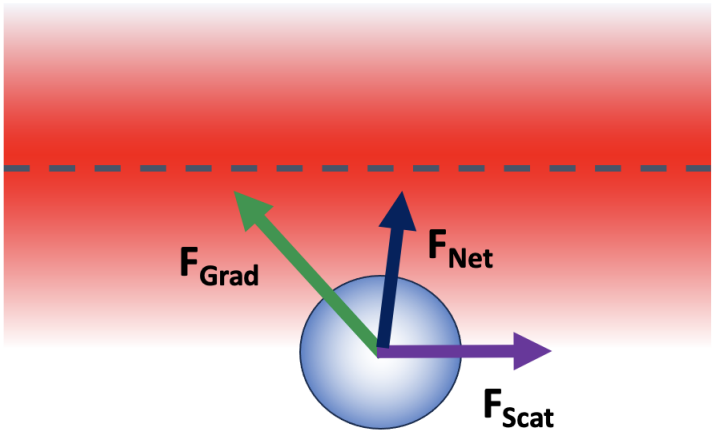

FIGURE 2.1: Forces generated on a bead within the Rayleigh regime for a focused laser beam ("Optical Tweezers").

$$F_{\text{grad}} = \frac{1}{2} n_m \alpha \nabla \mathbf{E}^2 = \frac{n_m^3 r^3}{2} \left(\frac{n_p^2 - n_m^2}{n_p^2 + 2n_m^2} \right)^2 \nabla \mathbf{E}^2 \tag{2.1}$$

$$F_{scat} = \frac{I_0}{c} \frac{128\pi^5 r^6}{3\lambda^4} \left(\frac{{n_p}^2 - {n_m}^2}{{n_p}^2 + 2{n_m}^2} \right)^2 n_m \tag{2.2}$$

2.1.1 Nanoaperture Trapping

Nanoapertures and other metallic nanostructures have been pivotal in the advancement of optical tweezers because of their ability to exert considerable radiation forces and significantly influence the local electric field [43]. Various structures such as metal tips [44], patterned surfaces [45], and especially nanoapertures [27], have emerged as key tools in this field. Nanoapertures have garnered significant interest for their ability to strengthen optical trap stiffness through the 'self-induced back-action' (SIBA) mechanism. This unique effect utilizes a nanoaperture to enhance the local electric field, while the presence of the trapped particle concurrently affects the optical transmission to maintain the trap, as outlined in Juan et al.'s 2009 study [46].

Juan et al.'s work not only confirmed the theory of SIBA but also demonstrated that particles under 100 nm could be trapped efficiently with lower laser power requirements [46]. This finding is built upon the theoretical groundwork laid by Okamoto and Kawata in 1999, which posited that particles near a nanoaperture are pulled towards it by the radiation force. This force is sufficiently strong to overcome gravity and thermal forces affecting the particle [47]. A key aspect of SIBA is the impact of the dielectric particle on aperture transmission. According to Bethe's aperture theory [48], when a particle with a refractive index higher than that of the surrounding medium enters a subwavelength aperture, it leads to an increase in the aperture's transmission:

$$T \propto \left(\frac{nr}{\lambda}\right)^4 \tag{2.3}$$

This formula signifies that the transmission change is directly proportional to the quadratic ratio of the particle's radius (r) and the wavelength of the light (λ), scaled by the refractive index of the particle (n). The resultant alteration in transmission leads to a corresponding shift in the photon flux and momentum through the aperture. If the trapped particle tries to escape the aperture because of scattering or thermal forces, the effective size and transmission of the aperture decrease. This, in turn, intensifies the optical forces exerted on the particle, propelling it back into the aperture and thus ensuring its optical entrapment.

Besides these effects, the Clausius-Mossotti factor (K) plays a crucial role in nano-aperture trapping by measuring the variations in the transmission level when the particle shifts from an untrapped to a trapped state. The factor can be calculated using the permittivity (ϵ) of the particle (p) and the surrounding medium (m):

$$K = \frac{\epsilon_p - \epsilon_m}{\epsilon_p + \epsilon_m} \tag{2.4}$$

This factor, K, is essential in understanding the relationship between the particle's properties and the changes in optical forces and transmission during trapping.

Moreover, studies have indicated that double nanoholes offer superior stability compared to single circular apertures for optical trapping [49]. Double nanoholes prompt nanoparticles to fluctuate between two points of minimal energy located at

the cusps of the aperture. This dynamic leads to more stable and efficient trapping, leveraging the unique properties of nanoapertures to enhance the performance of optical tweezers.

In conclusion, the integration of nanoapertures into optical tweezers represents a significant advancement in the field. By utilizing the unique properties of these structures, such as their ability to enhance trap stiffness through SIBA and the Clausius-Mossotti factor, researchers have been able to achieve more effective and stable trapping of nanoparticles, opening up new possibilities for manipulation and study of microscopic particles.

2.2 Nanothermometry in Nanoaperture Studies

Shaped nanoapertures have been instrumental in trapping a wide range of nanoparticles, from proteins and quantum emitters to other particles in the 1 nm to 50 nm size range [27], [46], [50]–[64]. In these environments, temperature control is pivotal, as it can influence the stability and behaviour of trapped entities. Laser-induced heating, for example, has been employed to elevate temperatures to physiological conditions, impacting the stability of proteins [62].

Thermophoresis can attract or repel particles based on their thermophilic or thermophobic nature, which is influenced by temperature and the surrounding

medium. This phenomenon has been utilized in nanoaperture studies to manipulate proteins and DNA [65]. Additionally, thermal-induced convection in microfluidic systems has proven effective in creating high-temperature gradients for delivery purposes [56].

2.2.1 Fluorescence Intensity Ratio

Local temperature monitoring within nanoapertures has been achieved through various methods, including fluorescence-based techniques. Researchers have observed an intensity-dependent temperature increase of 0.9 K/(mW/μm^2) by tracking the diffusion of fluorescently doped polystyrene nanospheres in a DNH setup [66]. Similarly, fluorescence correlation spectroscopy, intensity, and lifetime measurements have provided an accurate temperature profile in these studies, revealing temperature increases up to twice that measured in previous research due to increased absorption from the laser incident on the adhesion layer side [67], [68].

Ion current measurements have also been utilized, especially in structures like bowtie nanoapertures, where temperature increases of 3.6 K per 7.5 mW were reported [69]. These findings align with fluorescence-based studies, considering the diffraction-limited focus spot size in these wavelength ranges.

The fluorescence intensity ratio (FIR) method, particularly with lanthanide emitters, offers a unique and effective approach to temperature measurement. Lanthanides are beneficial because of their stable emission properties and their ability to withstand elevated temperatures. The FIR method, which employs fluorescence

intensity measurements from different thermally coupled energy levels, allows for simple and direct temperature determination. For instance, trapped upconverting nanoparticles (>100 nm) have been used to measure local temperatures in proximity to biological cells [70]. Thermally coupled energy levels refer to a pair or set of energy levels in an atom or molecule that are close enough in energy that thermal energy at a given temperature can promote population exchange between them. This means that at the temperature of the system, there is a significant probability that an electron can thermally transition between these levels. Thermally coupled energy levels are important for processes like non-radiative transitions and thermal quenching. The population of electrons in these levels can be temperature-dependent, which allows for applications such as ratiometric thermometry. Here, the ratio of fluorescence intensities from transitions starting from thermally coupled levels can be used to measure temperature since the ratio will change predictably with temperature due to the Boltzmann distribution.

Variations in excitation intensity or transmission losses in guiding fibers can lead to erroneous conclusions about temperature fluctuations. By measuring the fluorescence intensity from two different energy levels with distinct temperature dependencies, these potential errors can be mitigated. This dual-level measurement approach provides a robust means of monitoring temperature, independent of excitation intensity fluctuations or bend losses in fibers:

$$\text{FIR} = \frac{N_2}{N_1} = \frac{I_2}{I_1} = \left(\frac{g_2 s_2 \nu_2}{g_1 s_1 \nu_1}\right) \exp\left(\frac{-\Delta E}{kT}\right) \tag{2.5}$$

This equation includes several variables such as the number of ions N, fluorescence intensity I, degeneracy g, emission cross-section s, and angular frequency of fluorescence transitions from the upper (i=2) and lower (i=1) thermalizing energy levels to a terminal level j; ν, alongside the energy difference ΔE between two thermally coupled levels, the Boltzmann constant k, and the absolute temperature T [71]–[75].

The sensitivity of this method is determined by the difference in energy levels between the two states, as described by the equation:

$$S = \frac{1}{(FIR)}\left(\frac{d(FIR)}{dT}\right) = \frac{\Delta E}{kT^2} \tag{2.6}$$

The creation of a temperature sensor using the fluorescence intensity ratio (FIR) method requires the use of specific materials that have thermally coupled energy levels. Other factors, such as availability and cost, temperature ranges, and ease of obtaining fluorescence from the levels of interest, determine a material's suitability for developing a sensor. The trivalent form of rare-earth ions is a class of materials that satisfy the aforementioned criteria and have been traditionally employed in the fabrication of laser and amplifier materials. Other requirements for rare- earth ions include thermally coupled energy levels, a separation of more than $200\,\mathrm{cm}^{-1}$ to avoid overlap, and radiative transitions predominating nonradiative transitions. Furthermore, the excitation of fluorescence must be achieved through light sources

that are readily accessible. The rare-earth ions that satisfy the given criteria are praseodymium, promethium, neodymium, samarium, europium, dysprosium, erbium, and ytterbium [76], [77].

The current limitations of nanothermometry in micro- or nanoscale research include the following:

1) Temperature Resolution: Achieving high-temperature resolution at the nanoscale is a significant challenge. Nanothermometers need to provide accurate and precise temperature measurements, especially in biological systems, to understand fundamental properties and processes.

2) Biocompatibility: In the context of nanomedicine, ensuring the biocompatibility of nanothermometers is crucial. The materials used should not cause adverse effects in biological systems, and the detection procedures should be suitable for in vivo applications.

3) Sensitivity and Selectivity: Nanothermometers must exhibit high sensitivity and selectivity to changes in temperature, particularly in complex and dynamic environments such as living cells. This requires the development of materials and detection procedures that can accurately respond to temperature variations.

4) Imaging Techniques: Integrating nanothermometry with state-of-the-art imaging techniques poses challenges, as it requires the development of advanced imaging methods to achieve improved spatial, temporal, and temperature resolutions for monitoring temperature changes at the nanoscale.

5) Bias Sensing: There have been concerns about possible biased sensing during fluorescence-based detection, highlighting the need to address and mitigate potential sources of bias in nanothermometry techniques [78].

Addressing these limitations is essential for the continued advancement of nanothermometry, enabling its widespread application in diverse areas such as micro/nanoelectronics, nanomedicine, and high-resolution imaging studies.

2.2.2 Upconverting Nanoparticles

Upconverting nanoparticles (UCNPs), which consist of a host crystal doped with lanthanide ions like Er^{3+}, Yb^{3+}, Ho^{3+}, Gd^{3+}, and Tm^{3+}, represent a significant advancement in nanothermometry. These particles, often composed of metal fluorides ($NaYF_4$), oxides (Y_2O_3), phosphates (YPO_4), or vanadates ($GdVO_4$), are capable of emitting light at higher energies than the excitation wavelengths because of the process known as upconversion.

One of the key advantages of UCNPs is their minimal background fluorescence, because of the negative Stokes shift, making them ideal for high-resolution optical imaging. Since the early 1990s, UCNPs have been employed in temperature measurements, leveraging their thermal response mechanisms based on the sensitivities of various electronic transitions. For instance, Er^{3+}/Yb^{3+} doped $NaYF_4$ nanoparticles are used for ratiometric temperature evaluation by measuring the ratio of Er^{3+} ion green emission intensities between the $2H_{11/2}$ level (525 nm) and the $4S_{3/2}$ level (545 nm). The ability to be excited with low-power, near-infrared lasers enables UCNPs to penetrate deep into biological tissues, making them particularly suitable for biological systems [79], [80].

2.3 Single Photon Sources

Single photon sources, capable of emitting one photon at a time, are crucial for encoding quantum information in photons, thus creating 'photonic qubits'. These qubits, usually characterized by the photon's polarization or energy, are ideal for diverse quantum information science applications. Their minimal interaction with the environment, light-speed travel, and amenability to linear optical system manipulations make them highly suitable for these roles [81]. A variety of systems can serve as single photon sources, ranging from individual ions [25], [26], atoms [82], and molecules [83], to solid-state emitters like quantum dots [84] and color centers [85].

In single emitter systems, the mechanism generally involves an optical or electrical stimulus prompting the system into an excited state, which then relaxes to emit a singular photon. The emitter, upon excitation by a laser pulse, transitions from its ground state to an excited state, followed by the emission of a photon as it returns to the ground state. This radiative emission rate is limited by the excited state's duration and the time it takes to relax from the excited state to the ground state [86]. Quantum computing applications, particularly quantum teleportation techniques that involve transmitting and receiving quantum states, necessitate sources that can produce not just single photons but also maintain indistinguishability between consecutive photons [87].

2.3.1 Erbium

Erbium ions are an attractive option for single photon sources since they emit photons at low-loss fiber optic wavelengths [88]. Single photon sources can benefit from the steady emission and quantum state control of several rare-earth ions, such as Pr^{3+}, Ce^{3+}, and Er^{3+} [89]. A key aim of this study is to develop a single photon source based on rare-earth ions that operates efficiently in the low-loss infrared C-band (1530–1565 nm). This wavelength range is particularly significant due to the properties of Er ions, which are central to Er-doped fiber amplifiers (EDFAs) used in long-range telecommunications. Er ions emit light in this C-band and exhibit excellent quantum control characteristics, making them highly suitable for this application [90].

The 1.5 µm transition in EDFAs has been a cornerstone of long-distance optical fiber communications for many years, thanks to the unique optical properties of Er. These characteristics include various visual and NIR transitions, as depicted in Figure 2.2. The transitions encompass ground-state and excited-state absorption transitions (indicated by dashed lines) and intermediate phonon relaxation transitions (represented by curly lines), categorized by the $^{2S+1}L_J$ atomic term symbols, where S, L, and J denote the spin, orbital, and angular momentum quantum numbers, respectively. The relatively long lifetimes of the excited states of Er materials, typically on the order of 10 ms in most host crystals, limit the photon emission rate and consequently their brightness. However, Er's quantum state can be manipulated through coherent spin and optical transitions [91], which positions Er

as a viable candidate for quantum communication technologies. Moreover, the shielding provided by the $4f$ electrons, protected by the outer $5s$ and $5p$ electrons, reduces external phonon coupling. This protective effect persists even when Er is integrated into a solid-state host crystal [92].

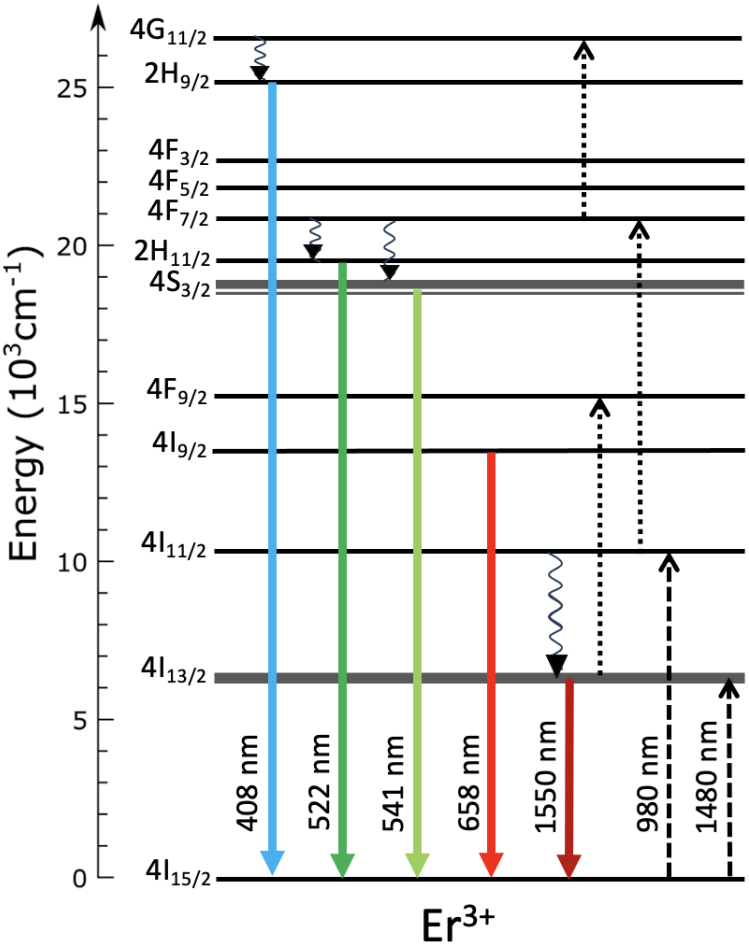

FIGURE 2.2: Erbium energy diagram, black solid lines showing absorption transitions, radiative transitions are shown by coloured solid lines, dashed lines show excited state absorption, and multiphonon relaxation is shown with curly lines.

2.3.2 Effective Parameters in Quantum Emission

Quantum emitters, such as fluorescent nanoparticles, can have their emission altered when they are optically confined. As a result of this interaction, the particle's spontaneous emission rate might increase as a result of the high density of optical states inside the limited volume, which is known as the Purcell effect [93]. Fluorescence quenching [86] is a term used to describe the phenomenon of emission rate reduction because of phonon coupling when the confinement is too near to the interface.

In a quantum emitter, emission takes place as a result of radiative relaxation. The rate of radiative decay is the limiting factor in this process. phonon vibrations, heat, and other undesirable coupling can also relax the system non-radiatively. Emission rates of an emitter can be affected by the surrounding environment [94]. The total emission rate increases if the radiative rate goes up, but the emission is quenched if the non-radiative rate increases. In this system the total quantum yield is defined by η_0, calculated as below:

$$\eta_0 = \frac{\gamma_r}{\gamma_r + \gamma_{\mathrm{nr}}} \tag{2.7}$$

γ_r is the radiative decay and γ_{nr} is nonradiative decay.

Metallic nanostructures have the potential to be engineered in a way that not only confines the quantum emitter but also makes use of plasmonic phenomena to boost the local electric field [86]. By increasing the concentration of the field, the

nanostructures can impact both radiative decay rates as well as non-radiative decay rates [94], [95]. According to Fermi's golden rule, the relaxation rate increases as a result of the increasing local field.

$$\gamma_{if} = \frac{2\pi}{\hbar} \left| \langle f | E \cdot p | i \rangle \right|^2 \rho_f \tag{2.8}$$

$\hbar$ represents the reduced Planck constant, E is the localized electric field, p denotes the transition dipole moment, and ρ_f is the electron density in the final states. Fluorescent particle excitation energy can be diverted into various non-radiative pathways, such as phonon coupling, particularly when emitters are positioned close to a particle's surface, like in lanthanide-doped nanocrystals [86]. This proximity can significantly impact quantum efficiency by converting excitation energy to other forms, absorbed by the surrounding environment instead of emitting photons [96].

Imagine a system where a light pulse activates a particle tightly linked to its environment. Here, the light pulse may be transformed into a phonon, transferring its energy outward. In scenarios like these, especially at interfaces or in densely coupled systems, various factors like heat, surface modes, and unwanted waveguide modes can siphon energy from radiative processes, leading to fluorescence quenching. This quenching can drastically reduce emission in quantum emitting nanoparticles, particularly when located near an interface or within certain mediums. Protecting active areas of nanoparticles with a passive coating can mitigate this effect and preserve fluorescence efficiency [97].

Phonon scattering adheres to a specific rate, termed the relaxation rate. Notably, quantum rate amplification due to confinement may not uniformly impact phonon relaxation rates as it does absorption and radiative rates. In the case of the Erbium ion system (illustrated in figure 2.2), a non-radiative transition from the ${}^4I_{11/2}$ level to the ${}^4I_{13/2}$ level is required when excited with 980 nm light, before returning to the ground state. This transition phase, potentially lasting microseconds, could limit an Er-based single photon source's operational frequency to the kilohertz range. An alternative approach involves exciting the system with 1480 nm light, promoting the system to a higher-energy virtual state, potentially reducing the lifespan of this state to just tens of nanoseconds. The nonradiative relaxation rate for such a system, A_{NR}^{-}, is computed using the formula [98]:

$$A_{NR}^{-}(T) = B[n(T) + 1]e^{-\beta \Delta E} \tag{2.9}$$

In this equation, B is a material-specific constant, $\beta = -\log(\varepsilon)/\hbar\omega$, ΔE is the energy gap, and $n(T)$ represents the Bose-Einstein occupation number of the phonon mode. While specific values for B and β for $NaYF_4$ are not established, literature often uses $LiYF_4$ as a close approximation, with $B = 6.4 \times 10^7$ s^{-1} and $\beta = 3.6 \times 10^{-3}$ cm [99].

2.3.3 Anchoring Nanoparticles on Gold Surfaces

In this dissertation, we explore innovative methods for anchoring nanoparticles to gold nanostructures by harnessing the chemistry of gold-thiol bonding and photochemical protection. These techniques play a crucial role in creating stable nanoassemblies with specific functionalities.

Thiol-Gold Surface Bonding

The process of gold-thiol bonding plays a crucial role in securing thiol groups to gold surfaces, a phenomenon driven by the strong affinity between sulphur atoms and gold. This reaction commences when a molecule, adorned with a thiol (-SH) end group, adheres to a gold surface. Initially, the thiol group establishes a weak physical bond, known as physisorption, with the gold. This bond evolves into a more enduring Au-S bond as a result of chemisorption, where the S-H bond is broken and reformed with gold.

Gold-thiol bonding's application extends well beyond mere attachment; it's a fundamental technique in nanofabrication, particularly in the creation of self-assembled monolayers (SAMs) of organic molecules. By altering nanoparticle surfaces to include thiol end-groups, these nanoparticles can be efficiently anchored to gold surfaces, harnessing this strong chemical bond.

UV-Triggered Photochemical Bonding

Photochemical protection is another fundamental technique utilized in our research. It involves the use of photoremovable groups to shield certain functional groups in a molecule until they are exposed by a specific photochemical reaction. Ultraviolet (UV) light, with its high photon energy, is commonly employed as a trigger for these reactions.

Here, we delve into the specifics of the photochemical reaction associated with the photoremovable protecting group, 2-bromo-4'-hydroxyacetophenone. This particular group is attached to nanoparticles that are coated with DSPE-PEG-SH layers, a crucial aspect of the experiments described in Section 3.1.4. While the precise bonding dynamics of this group to the nanoparticle surface remain a subject of ongoing research, we explore the reactions attributed to p-hydroxyphenacyl (pHP), a probable resultant group, to gain a better theoretical understanding.

The realm of photochemical protection finds its applications across diverse fields, notably in biology. The pHP group is especially noteworthy for its quick-release properties. It has been effectively utilized in applications such as the rapid, light-triggered discharge of bioactive phosphates and the swift activation of biological receptors. Additionally, this method has found utility in UV-induced thiol-yne 'click' reactions, a process where a photochemical response facilitates the bonding of surface-modified particles to corresponding substrates.

2.4 Erbium Doped Silica Microresonator

Low threshold and narrow linewidth lasers may be built using WGM microresonators because of their low optical losses (i.e., high Q) and very small sizes (i.e., small V). Microscale WGM resonators may now be manufactured from a wide range of materials and forms because of advancements in fabrication technology. Different resonators have been described, such as water droplets, silica, semiconductors, etc. As a result, a wide variety of shapes and geometries have been proven and employed in applications as diverse as sensing to microcavity lasers and more. Either active materials are introduced into the resonator or intrinsic nonlinearities of the resonator material are used to lase in WGM resonators. The combination of high Q resonators and various gain materials, including, quantum dots, and rare-earth ions, results in a wide range of laser topologies that may be used in several wavelengths, from ultraviolet to infrared. These pioneering efforts on microlasers in diverse materials and the current status of the area are briefly discussed in this section. The capacity to create brief pulses and a wide emission spectrum combined with excellent efficiency and a lengthy upper-level lifespan has made Er^{3+} one of the most popular dopants used for making active media for lasing purposes. Sol-gel technique is an efficient method for adding the dopants to different media. One way to achieve lasing at 1550 nm wavelength is to pump Er^{3+} ions with the 980 nm band. Non-radiative decay to the ${}^4I_{13/2}$ metastable level occurs when ions are heated from ground level ${}^4I_{15/2}$ to excited level ${}^4I_{11/2}$ using a 980 nm pump laser. They subsequently transit back to ${}^4I_{15/2}$, emitting photons

near 1530 nm.

2.4.1 Sol-gel Process

Silica as a compound has many remarkable properties because of its good transmittance in the visible region and chemical stability, which makes it suitable for thin film applications in photonic devices including lasers and sensors [100]. The sol-gel technique is a cost-efficient, rapid, and versatile wet-chemical synthesis approach used to make glasses and ceramics.

The sol-gel process describes the transformation of a colloidal solution (known as a "sol") into a more solid "gel" state. This method often begins with metal salts or metal-organic compounds, such as metal alkoxides, as the initial substances. Through hydrolysis and condensation reactions, these precursors evolve into a colloidal suspension or "sol." Subsequently, the particles within the sol coalesce, forming a gelatinous, continuous liquid phase or "gel." The process proceeds with additional drying and heating phases, during which the gel solidifies into a dense ceramic or glass structure.

Throughout the sol-gel process, three key chemical reactions take place: hydrolysis, alcohol condensation, and water condensation. The use of alcohol as a co-solvent is crucial in mixing alkoxides with water, aiding the hydrolysis process. In this reaction, water acts to replace alkoxide groups (OR) with hydroxyl groups (OH). These newly formed silanol groups (Si-OH) undergo further condensation to create siloxane bonds (Si-O-Si), resulting in either water or alcohol as byproducts.

As the formation of siloxane bonds progresses, they link together, building a silica network. Within this network, the trapped solvents gradually evaporate, and the organic residue is eliminated through high-temperature treatment. This leads to the collapse of interconnected pores, culminating in the formation of a dense glass or ceramic material [101]–[103].

Hydrolysis and Condensation

The hydrolysis of metal alkoxides can indeed occur without a catalyst, but the presence of an acid or base catalyst can significantly enhance the speed and extent of the reaction. This is because an acidic medium (in an acid-catalyzed reaction) provides protons that can be absorbed by the oxygen atom of the Si–OR group, leading to rapid protonation of the alkoxide group. As a result, the silicon atoms become positively charged due to the movement of electrons from these atoms to the oxygen atoms. This reaction increases the electrophilicity and reactivity of the silicon atoms toward water molecules in the hydrolysis process or silanols in the condensation reactions. The increased reactivity of the silicon atoms leads to a faster hydrolysis of the unreacted alkoxide (Si–$(OR)_4$) compared to the partially hydrolyzed ($Si(OR)_4$–x$(OH)_x$) or condensed (–Si–O–Si–) species. The presence of more Si–O–Si bonds increases the acidity of the silanol groups as condensation progresses1 4. The acid-catalyzed mechanism can be described as follows: (1) The acid catalyst donates a proton to the oxygen atom of the alkoxide group, leading to the formation of a positively charged silicon atom and a negatively charged oxygen atom.

(2) The positively charged silicon atom then reacts with a water molecule, leading to the formation of a silanol group and the release of an alcohol molecule. (3) The silanol groups can then undergo further condensation reactions to form Si–O–Si bonds, releasing water in the process. The specific reactions are as follows:

(1) Acid-catalyzed protonation $\mathrm{Si(OR)_4 + H^+ \longrightarrow [Si(OR)_4H]^+}$

(2) Hydrolysis $\mathrm{[Si(OR)_4H]^+ + H_2O \longrightarrow Si(OR)_3(OH) + ROH}$

(3) Condensation $\mathrm{2\,Si(OR)_3(OH) \longrightarrow (OR)_3Si-O-Si(OR)_3 + H_2O}$

These reactions are general and can be applied to other metal alkoxides as well, not just silicon alkoxides [104].

Gelation

The gelation process involves the condensation reaction of the alkoxide gel precursor, which produces water or alcohol. This reaction is also influenced by the presence of an acid or base catalyst. With the presence of an acid catalyst, a weakly crosslinked polymer is formed, which can easily aggregate and yield a microporous structure with low porosity after drying.

Water-Releasing Condensation $\mathrm{Si(OH)_4 \longrightarrow SiO_2 + 2\,H_2O}$

Alcohol-Releasing Condensation $\mathrm{Si(OR)(OH)_3 \longrightarrow SiO_2 + ROH + H_2O}$

Aging

Following gelation, the aging stage is critical because it involves ongoing chemical and physical transformations. As the process progresses, more cross-links are

formed, causing the gel to contract as covalent bonds replace non-bonded interactions. Furthermore, as the gel structure evolves, the size of the pores and the strength of the pore walls change.

Drying

The gel is made up of a lot of water and a network of interconnected three-dimensional pores. Densification requires drying the gel to remove the liquid trapped in the pores before they close. However, removing liquid from small pores can cause significant stress because of uneven shrinkage, resulting in structural cracking. This is a significant issue that must be addressed to avoid cracking during drying, particularly for larger monolithic objects larger than 1 cm in size. Controlling the chemistry at each processing step is critical to avoiding catastrophic cracking during drying in ambient conditions. Smaller structures, such as powders, coatings, or fibers, on the other hand, can withstand the drying stress without any special precautions.

Densification

While sol-gel silica can be used for a variety of applications at or near room temperature (including the entrapment of biological or organic molecules in its pores), dense ceramics or glass must be annealed at high temperatures. The pores are removed during this process, and the sol-gel materials become as dense as fused

glass. The temperature required for densification varies depending on factors, such as pore size and degree of connection, as well as material surface area [24].

Under benign conditions, the sol-gel method provides significant flexibility in the fabrication of glass and ceramics. Its benefits are well-documented, and they include [105]: The sol-gel process uses a wet chemical synthesis method, which allows for precise molecular-level composition customization. This makes precise stoichiometric and homogeneous control of dopants within the material possible. The use of liquid precursors allows the creation of glass and ceramic products in a variety of forms, such as thin films, fibers, and monolithic structures. This variety is possible without the use of traditional machining or melting techniques.

Incorporating Er ions into the forming silica lattice via sol-gel processing involves a delicate interplay between the silica network formation and the introduction of Er^{3+} ions from Erbium(III) nitrate pentahydrate ($Er(NO_3)_3.H_2O$). As the silica network forms through the hydrolysis and condensation of the silica precursor, the Er^{3+} ions are integrated into the lattice. This occurs concurrently with the gelation process, where the erbium ions are entrapped within the porous silica matrix. During the subsequent aging and drying processes, these ions find equilibrium positions within the silica network, often associated with oxygen defects or non-bridging oxygen sites which facilitate their incorporation and ensure their stable placement within the matrix.

The precise positioning of Er^{3+} ions is influenced by the silica matrix's evolving

microstructure, which undergoes further densification and homogenization during the annealing stage. This step is crucial as it allows Er ions to settle into the more energetically favourable sites within the silica lattice, ensuring optimal optical properties for photonic applications. The sol-gel process's inherent control over the dopant concentration and the homogeneous distribution of the dopants is what makes this method particularly advantageous for crafting high-quality Er-doped materials suitable for a wide range of photonic applications.

2.4.2 Quality Factor Measurement

The quality factor or Q factor of a microresonator, is a measure of the resonator's ability to store and release energy. It is defined as the ratio of the energy stored in the resonator to the energy lost per cycle. There are several methods to calculate the Q factor of a microresonator. One prevalent method involves using a tunable laser and a high-resolution spectrometer to measure the resonator's transmission spectrum. By scanning the laser across the resonance frequency and recording the transmission spectrum, the bandwidth of the resonance, (Δf) and resonant frequency (f) can be obtained. The Q factor is then calculated using the formula:

$$Q = \frac{f}{\Delta f} \tag{2.10}$$

Another method is to use a pulsed laser and a fast photodetector to measure the decay time (τ) of the resonator. The Q factor is then calculated using the formula:

$$Q = \frac{\pi f \tau}{2} \tag{2.11}$$

In this context, the decay time is related to the linewidth's full width at half maximum (FWHM) by:

$$\Delta f = \frac{1}{\pi \tau} \tag{2.12}$$

Each method has its advantages and disadvantages, which depend on the specific characteristics of the resonator and the experimental setup. For accurate and reliable Q factor measurements, it is crucial to carefully calibrate the measurement setup and account for any sources of noise or systematic error [106], [107].

Chapter 3

Experimental Methods

This chapter describes the experimental methods used to investigate the properties of Er-doped nanocrystals and also the synthesis of Er-doped silica thin film which is required for microresonator fabrication. We examined the behaviour of nanocrystals using optical trapping and spectroscopy, emphasizing the use of nanofabricated structures and a photochemical approach for nanocrystal anchoring. The thin film synthesis procedure included an extensive set of steps that included thin film deposition and advanced fabrication techniques. The details of these experimental procedures are discussed in the following sections.

3.1 Erbium in nanostructure

This project involves utilizing optical trapping methods using nano aperture optical tweezer to explore the potential applications of Er-doped nanocrystals. Specifically, the project includes four experiments that aim to investigate the properties

and behavior of these nanocrystals. The following sections will outline each experiment and its respective goals.

3.1.1 Nano Aperture Fabrication

The nano apertures used in this experiment were made with a method called colloidal lithography, a relatively fast and low-cost method used by other members of our group [108]. In this technique, polystyrene nanospheres (500 nm) are diluted in ethanol to reach the desired concentration i.e. 0.01% w/v, drop coated the colloid on a 1.5 mm glass slide which was thoroughly cleaned using ethanol sonication, and left overnight to evaporate. At this step, a colloidal mask with different types of polystyrene colloids e.g. single, double, triple, etc. is formed. The next step is plasma etching, which changes the size of the nanocrystals that were deposited. Then, using Mantis QUBE sputtering system (shown in Figure 3.1), a 7 nm titanium as an adhesion layer and three different thicknesses of gold layer i.e. 70 nm, 100 nm, and 130 nm were sputtered on top of the substrate. As the final step, the polystyrene spheres were removed from the mask surface by either using sticky tape or sonicating the mask in ethanol for 8 minutes. The procedure is shown in Figure 3.2. Figure 3.4 and Figure 3.3 show SEM pictures of a fabricated nanoholes using 500 nm polystyrene beads.

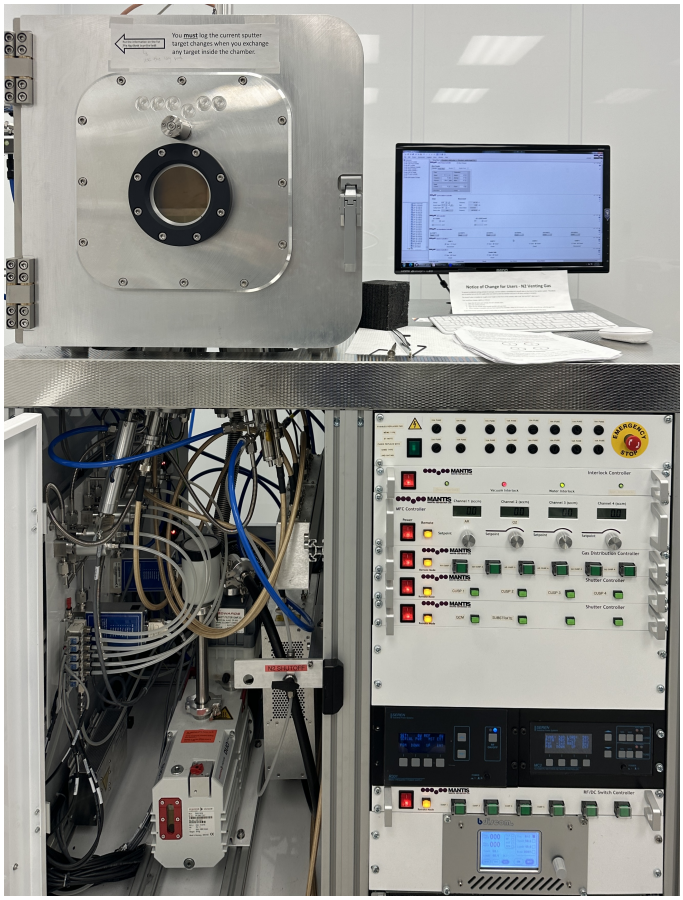

FIGURE 3.1: Mantis QUBE sputtering system.

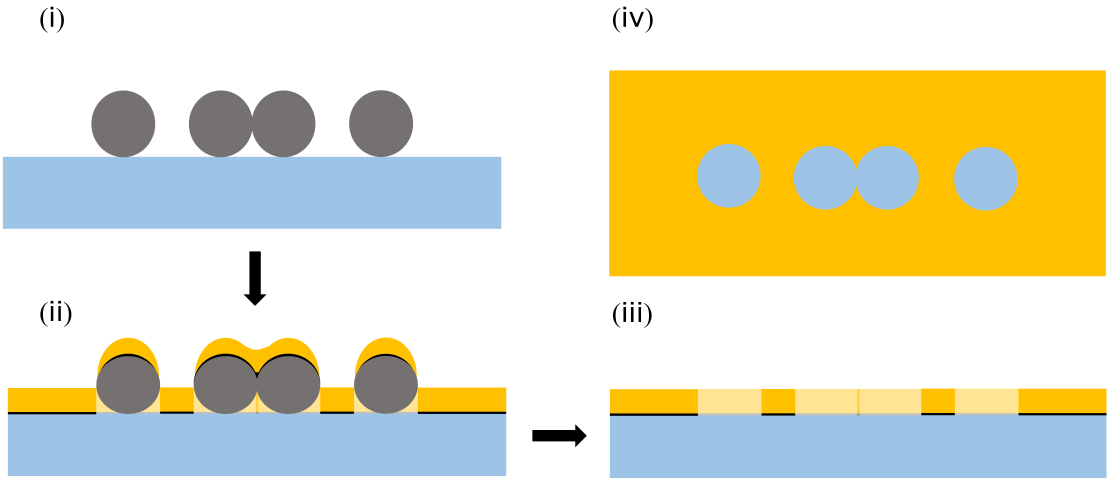

FIGURE 3.2: Colloidal lithography fabrication process steps. i) Polystyrene spheres were drop-coated on a glass slide. ii) The desired thickness of gold with a 7 nm titanium adhesion layer coated over the slide. iii) Spheres were removed by Sonication/tape. iv) Top view of the fabricated sample containing single and double nanoholes. Adapted with permission from [108] ©2019, Optical Society of America

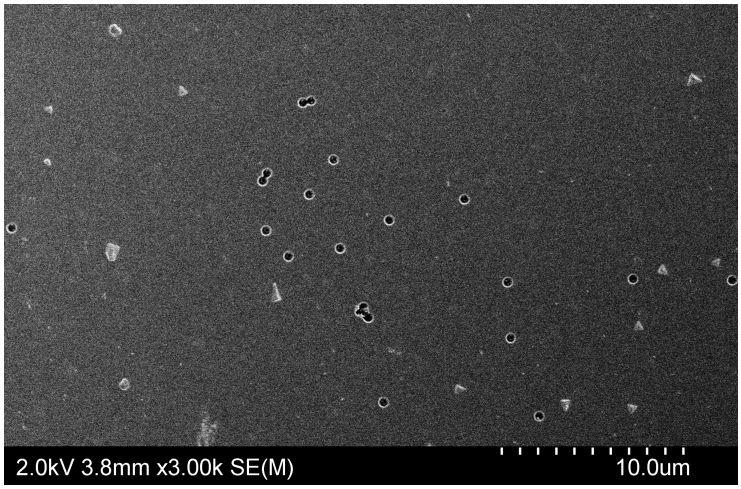

FIGURE 3.3: SEM picture of the fabricated sample containing double and single nanoholes.

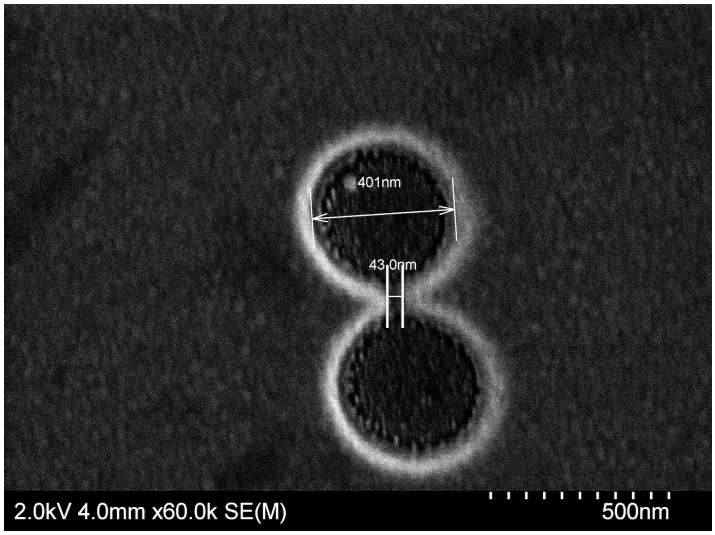

FIGURE 3.4: SEM picture of fabricated double nanohole using 500 nm polystyrene beads.

3.1.2 Nanocrystal Synthesis and Characterization

Er-doped $NaYF_4$ nanocrystals were synthesized by our collaborators in chemistry department. The characteristics of $NaYF_4$ as a host crystal have previously been investigated for a variety of lanthanide dopants such as Tm, Er, Yb, etc.[109].

High Concentrion Er-doped Nanocrystals For Nanothermometry:

We chose $NaYF_4$ nanocrystal as the host lattice because it enables for very effective yttrium substitution with erbium dopant and possesses low energy phonon modes [92],[110]. Nanocrystal synthesis used Yttrium(III) chloride hexahydrate (99.99%), erbium(III) chloride hexahydrate (99.995%), ytterbium(III) chloride hexahydrate (99.998%), ammonium fluoride (99.99%), tech grade oleic acid (90%), tech grade 1-octadecene (ODE, 90%), and hexane were purchased from Sigma-Aldrich. Anhydrous ethanol from Commercial Alcohols, methanol from Caledon, and sodium hydroxide from Bio Basic Canada Inc. were used. All chemicals were used as received. Up-converting nanocrystals were synthesized according to previously reported procedures [111]. Briefly, In a 100 mL three-neck round-bottom flask, 0.8 mmol of $YCl_3{\cdot}6(H_2O)$, 0.18 mmol of $YbCl_3{\cdot}6(H_2O)$, and $ErCl_3{\cdot}6(H_2O)$ were accurately measured and introduced. The mixture was then combined with 15 mL of 1-Octadecene and 6 mL of oleic acid. It was stirred moderately, ensuring the liquid surface remained flat. Gradually, over 45 minutes, the mixture was heated to 140°C using a heating mantle under vacuum conditions, where it was maintained for one hour. During this process, the mixture became clear and slightly yellow in color. After cooling to 60°C over a quarter of an hour, a solution containing 15

mL of methanol, 2.5 mmol of NaOH, and 4 mmol of NH_4F was carefully added drop by drop. The mixture was then heated to 70°C and held until the methanol fully evaporated, taking approximately 30 minutes. Subsequently, the temperature was increased to 299°C for 15 minutes, then maintained at this level for 90 minutes. Post-heating, the mixture was left to cool down to ambient temperature. The mixture was then transferred to a centrifugation tube containing 30 mL of ethanol and centrifuged at 3000 g for 10 minutes. The supernatant was discarded, leaving a pellet at the bottom of the tube, which was then re-dissolved in 20 mL of hexane.

For nanocrystal size analysis, digital imaging techniques were employed. Using ImageJ software (version 1.52p), the surface area of at least 1000 particles was determined, from which the corresponding diameter was calculated. Average diameters and standard deviations were computed using Origin 2020 software. X-ray diffractograms with a resolution of 0.0263° were obtained with a PANalytical Empyrean X-ray System equipped with a Cu source (K radiation, = 1.54060) and operating at 45 kV and 40 mA. Figure 3.5 shows the size distribution extracted from the TEM image (shown in Figure 3.6). TEM images were captured using an 80 kV JEOL JEM-1400 microscope. Figure 3.7 shows the x-ray diffraction analysis for the synthesized nanocrytals. The nanocrystals synthesized in this work were of ca. 20 nm diameter with 18% Yb^{3+} and 2% Er^{3+}.

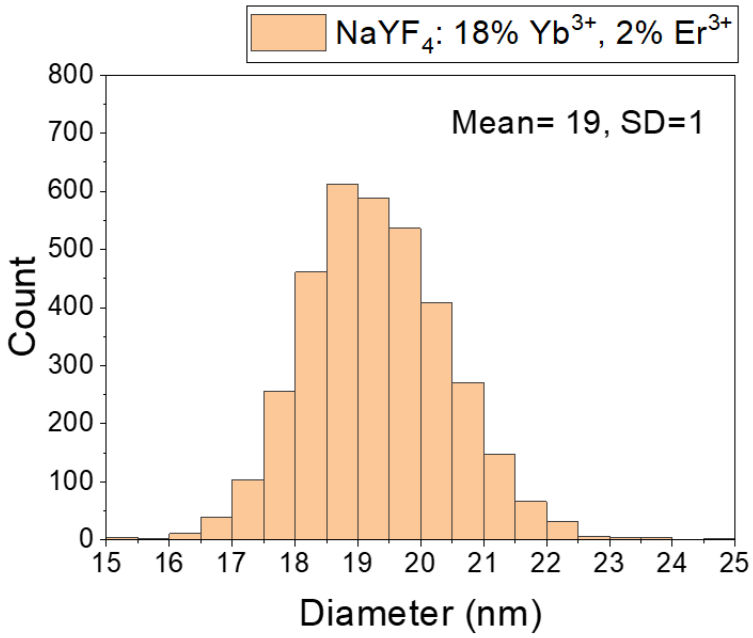

FIGURE 3.5: Size distribution diagram of the synthesized upconverting nanocrystals.

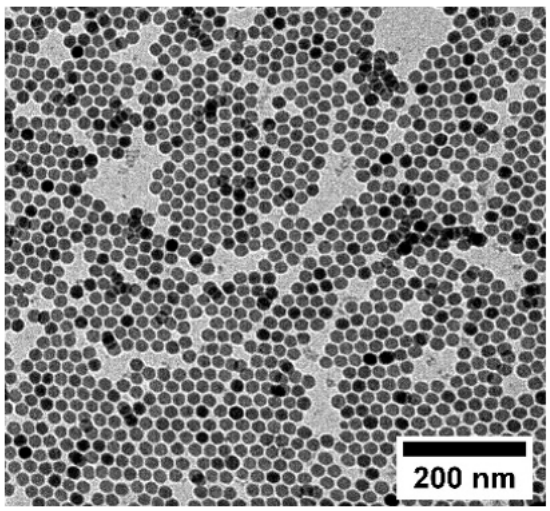

FIGURE 3.6: TEM image of the synthesized $NaYF_4$ nanocrystals

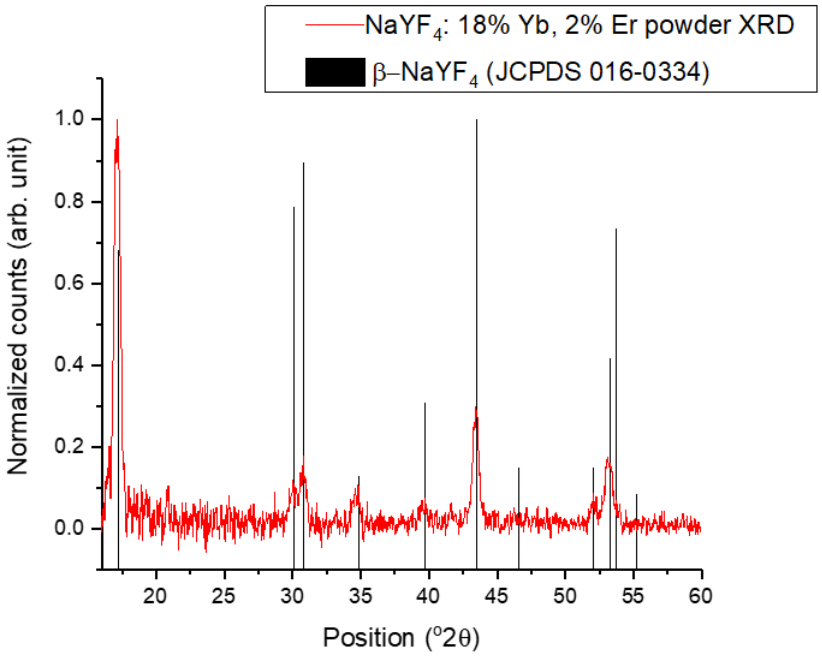

FIGURE 3.7: X-ray diffraction pattern of the synthesized upconverting nanocrystals.

Low Concentration Er-doped Nannocrystals For Anchoring:

The chosen host lattice was the same as the previous experiment i.e. $NaYF_4$. The surface of these particles was caped with oleic acid with 1nm thickness, DSPE-mPEG, and DSPE-PEG-SH protected by 2-Bromo-4'-hydroxyacet-ophenone as the photoremovable agent which can be removed by getting exposed to UV light. By removing the protective group, nanocrystals can be anchored to nanoapertures on the gold surface. To examine the characteristics of nanocrystals with discrete levels of emitters, the nanocrystals can be doped with low quantities of erbium. 26.1 nm $NaYF_4$ nanocrystals doped with an average of 2.5 Er ions/nanocrystal. Doping levels per nanocrystal has Poisson distribution with ca. 8% 0 Er, 20% 1 Er, 25% 2 Er, 20% 3 Er etc. Drop-cast nanocrystal dispersions in hexane were dropped onto a

form var carbon-coated grid (300 mesh Cu) and air-dried for about 1 minute before imaging [28]. Also other nanocrystals were utilized for testing since they exhibit consistent behaviour that may be used to check the trapping setup's functionality. Polystyrene beads and hexagonal boron nitride (hBN) nanoflakes were chosen for this purpose. The trapping signal from hBN nanoflakes in ethanol is shown in Figure 3.12.

3.1.3 Sample Packaging and Trapping Experiment

Sample Packaging for Nanothermometry Experiment

The initial solution of Er-doped nanocrystals in hexane media (17.6 mg/mL) was diluted to a concentration of 1.3×10^{12}/mL. An adhesive spacer with a thickness of 0.12 mm (Grace Bio-labs, SecureSeal) was put on a #0 glass coverslip to make a reservoir. Then the sample for optical tweezer measurement was prepared using 17.6 µL of the nanocrystal solution pipetted in the reservoir and the gold nanoaperture film was put on top of the reservoir with its face down. The packaged sample is shown in Figure 3.8.

Sample Packaging for Attachment Experiment

An aqueous solution of Er-doped nanocrystals was put in a package with the nanoapertures. As described earlier, the sample for optical tweezer measurement was prepared using 10 µL nanocrystal solution put in an adhesive spacer attached to a glass coverslip and sealed with the DNH containing gold-coated slide.

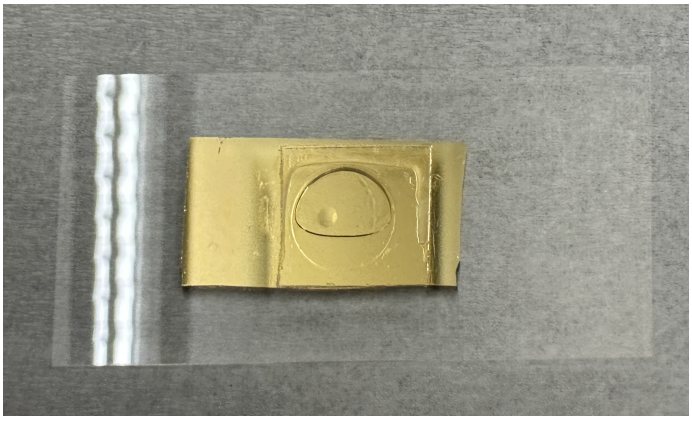

FIGURE 3.8: Er-doped nanocrystal solution packaged sample.

The next step is optical trapping, i.e. trapping the Er-doped particles inside a DNH by focusing a laser into an aperture and measuring transmitted light through that using avalanche photodetector (APD).

3.1.4 Trapping Experiment

In this study, we employed an advanced optical trapping method, using an optical tweezers setup with an inverted microscope, as shown in Figures 3.9 and 3.10. The setup utilized a 980 nm continuous-wave laser (JDS Uniphase SDLO-27-7552-160-LD), which was meticulously focused onto the sample with the aid of a 100× oil immersion objective lens. This system's design allowed us to precisely adjust the laser power, which ranged between 2 to 30 mW, contingent upon the aperture size used. These power measurements were recorded after the laser light passed through the 100X objective.

During our experimental setup, gold double-nanohole (DNH) apertures were the focal point of the study. These apertures were meticulously aligned with the

laser beam using an advanced three-axis stage, which boasted a fine-tuning capability of 20 nm resolution via piezo adjustment. This precise alignment was critical to enhance the transmission amplitude of light through the apertures. After achieving optimal alignment, the transmitted light was collected through a 10X microscope objective, and its intensity was precisely quantified using an avalanche photodetector (Thorlabs APD120A). This setup was also designed to capture light emissions from the trapped nanocrystals. The power spectrum of the reflected light was scrutinized using a spectrometer positioned on the reflection path, with a filter in place to exclude the input laser light. To accommodate different experimental needs, we alternated between a bifurcated fiber and a flip mirror. This setup allowed for the segregation of visible and near-infrared (NIR) spectra, directing them to two separate spectrometers. The visible spectrum, ranging from 350 to 1130 nm, was measured by an Ocean Optics QE65000 spectrometer. The NIR spectrum, covering 890 to 1760 nm, was captured using a Bay Spec NIRS0900-1700 spectrometer. To minimize thermal background noise, we ensured a 30-minute cooling period for the spectrometer before starting the measurements.

The Er-doped $NaYF_4$ nanocrystals were prepared with a polymer coating that included thiol end groups known for their rapid binding to gold. These nanocrystals were coated with a photoremovable group, 2-bromo-4'-hydroxyacetophenone to prevent immediate adhesion to the gold surface. Upon UV exposure, this group detaches from the nanocrystal, unveiling the thiol group and enabling the particle

to attach to the gold surface securely. This approach was critical in our investigation of isolating single Er emitters in a controlled manner for enhanced emission studies. For imaging, we employed a green light source operating at 550 nm. This particular wavelength was chosen to prevent premature initiation of the photochemical reaction, given that it is above the absorption band of the photoremovable group, which is activated at wavelengths below 360 nm [112]. In parallel, UV light at 340 nm was precisely focused onto the DNH using the 10X objective to trigger the photochemical reaction, while blocking any non-essential UV light.

To perform the anchoring experiment, the same nanocrystals were trapped and excited using the 980 nm laser. To optimize the transmission through the DNH, we made necessary adjustments to the orientation of the polarizer. Successful trapping within the water medium was confirmed by the observation of a distinct jump in the transmission signal, as depicted in Figure 4.12. After the trapping phase, the downshifting luminescence of the Er-doped nanocrystals was closely analyzed through NIR spectroscopy.

The anchoring process began with the optical trapping of a particle, as confirmed by the APD transmission signal. The UV light was then turned on for a pre-determined period to enable the attachment of the trapped nanocrystal inside the gold aperture. This exposure was critical as it led to the detachment of the photoremovable group from the nanocrystal, thereby exposing the thiol group and facilitating its binding to the gold surface inside the aperture. The laser was kept active even after the UV exposure to allow adequate time for the photo-reactive

group to bond firmly to the gold. Upon completion of the experiment, the sample was immersed in an IPA bath for 12 hours, effectively separating it from the spacer and microscope slide. The sample was then thoroughly cleaned with IPA and dried using nitrogen. Finally, SEM was used to image the DNH samples, both before and following the anchoring process, to validate the successful anchoring of the nanocrystals. Figure 4.13 shows electron micrographs of the anchoring process, with gold DNH apertures before and after the event.

Further building upon this setup, Figure 3.11 illustrates the process of trapping $NaYF_4$ nanocrystals in a water solution being trapped in a DNH. The APD in our setup captured the transmission through the aperture, with notable changes observed upon successful trapping of a particle. This change in transmission, known as the 'jump height,' was found to vary depending on the particle size and refractive index.

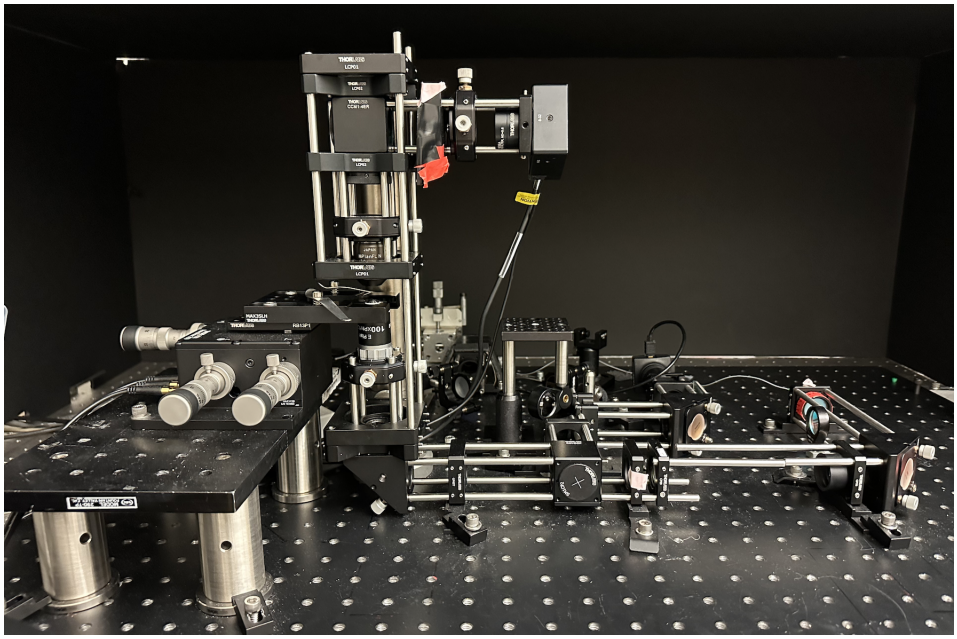

FIGURE 3.9: Optical trapping setup.

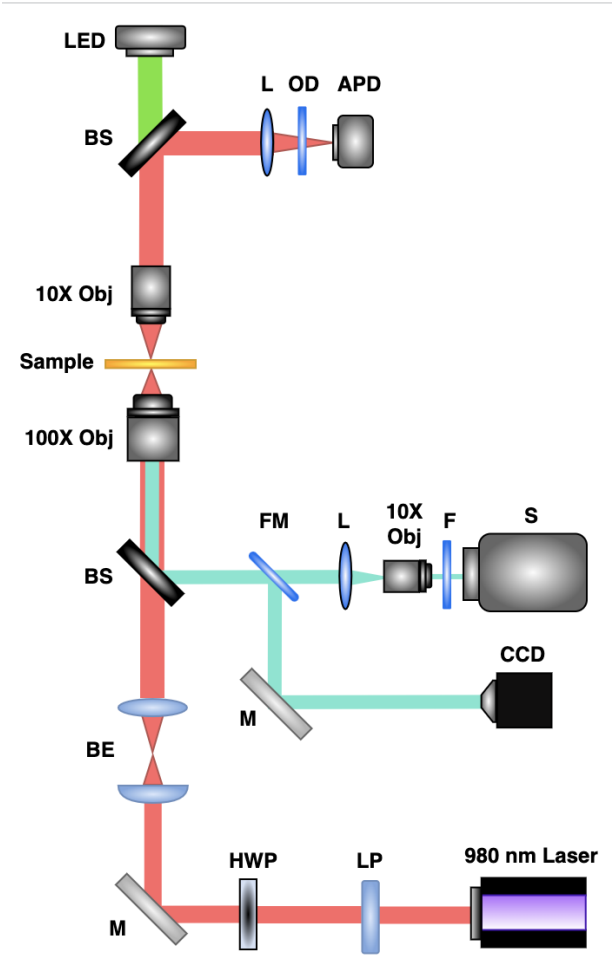

FIGURE 3.10: Schematic of optical trapping setup: CCD camera = charge-coupled device camera, LP = linear polarizer, L = lens, HWP = half-wave plate, BE = beam expander, BS = beam splitter, M = mirror F = filter, FM = flip mirror, Obj = objective lens, ODF = optical density filter and APD = avalanche photodiode, S = spectrometer.

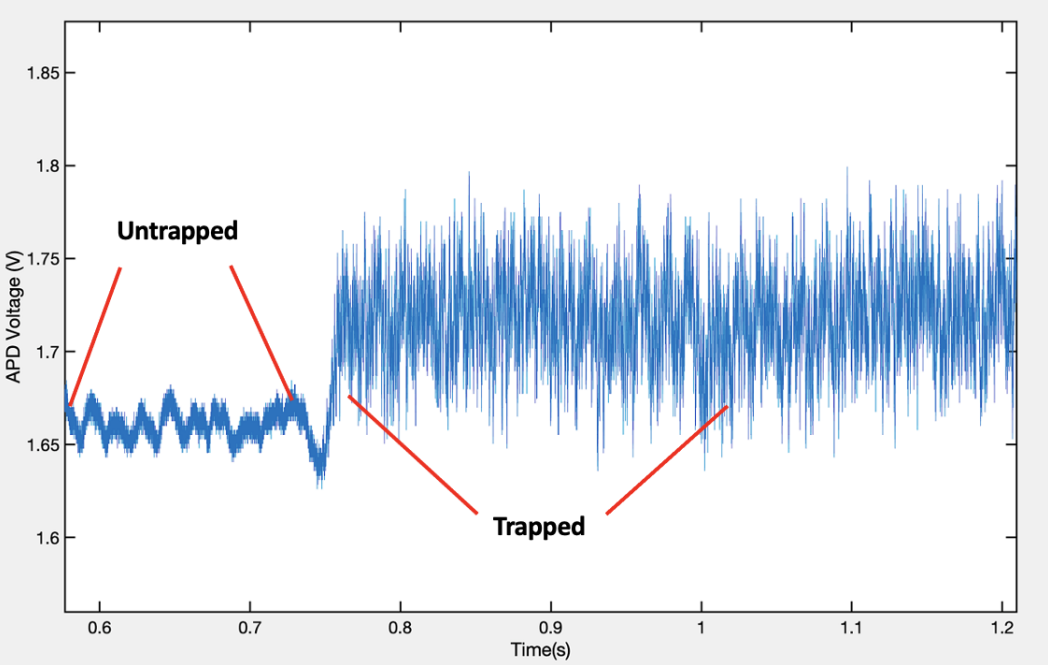

FIGURE 3.11: Trapping signal from $NaYF_4$ nanocrystals in water measured by APD.

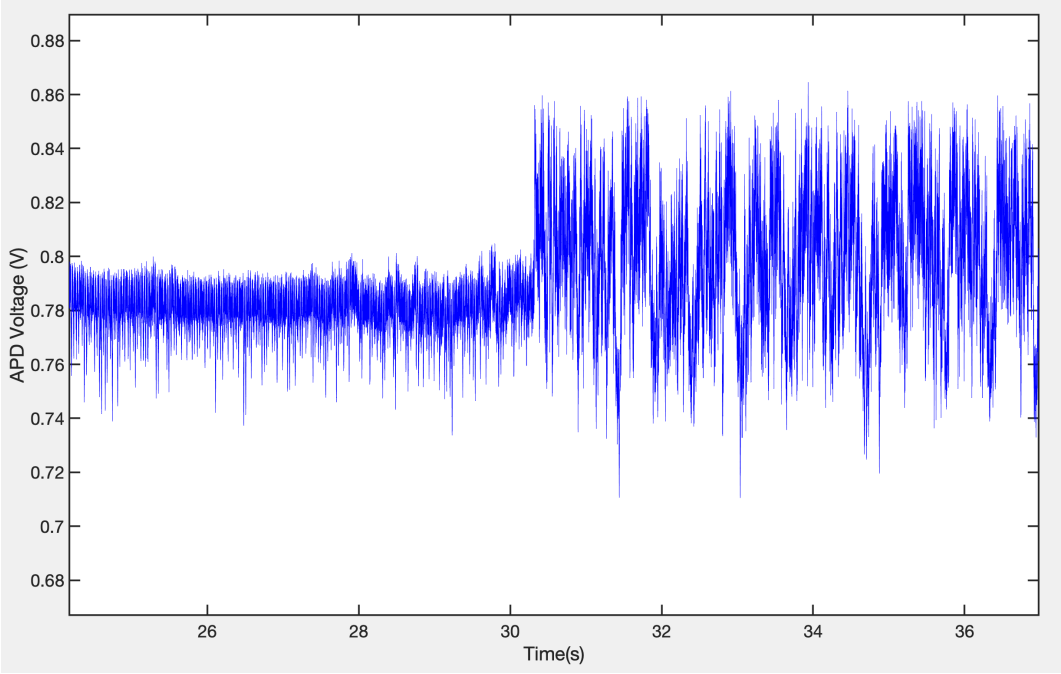

FIGURE 3.12: Trapping signal from hBN nanoflakes in ethanol.

For conducting the nanothermometry experiment, high-concentration Er-doped $NaYF_4$ nanocrystals were examined using the same setup, only this time trapping was done in hexane media. Figure 3.13 illustrates the trapping signal of a 20 nm $NaDyF_4$ nanoparticle, a material similar in composition to $NaYF_4$, suspended in hexane. This tracing was conducted to closely compare trapping dynamics and to validate the setup's ability to trap particles under these specific conditions effectively. The main graph shows a time series of the voltage measured by APD, which is indicative of the trapping event.

When utilizing non-polar solvents like hexane for optical trapping, the presence of significant oscillations upon laser activation serves as a hallmark of successful trapping [113]. This oscillatory behavior, distinctively observed in hexane, is absent in aqueous environments and cannot be attributed to the electronics of the monitoring circuit. It is hypothesized that these oscillations may arise from the interplay between hydrodynamic forces and the optical trapping potential, though a comprehensive analysis of this phenomenon remains unexplored. The inset provides a magnified view of the trapping event, highlighting the oscillation in voltage that corresponds to the successful stabilization of the nanoparticle in the trap. This detailed observation allows for a close comparison with previous trapping events, ensuring the reliability and precision of the experimental setup for trapping particles in hexane.

For the nanothermometry experiment, we utilized Er-doped nanocrystals with a high concentration for trapping. Initially, we captured a single nanocrystal using

a base laser power. Once the nanocrystal was securely trapped, we incrementally increased the laser power in stages. The APD signal variation corresponding to the rising laser intensity for a single trapped nanocrystal is depicted in Figure 4.2. Concurrently, at each of these incremental stages, we collected a spectrum, as illustrated in Figure 4.4 (b). This analysis specifically focuses on the wavelengths of 527 nm and 542 nm. Figure 4.4 (a) displays the energy level diagram for Er^{3+} and Yb^{3+} ions. In this diagram, an upconversion process is shown, where the energy from the Yb^{3+} transition is transferred to the Er^{3+} emitters, effectively boosting the excitation efficiency.

To verify that the spectrum we obtained originates specifically from the trapped nanocrystals and not from the surrounding bulk solution, we conducted a comparative test as validation. Figure 4.3 presents the emission spectrum resulting from the trapping of a nanocrystal in a solution with a dilute concentration of 1.3×10^{12} /mL. To establish a comparative baseline, a control experiment was conducted using a continuous gold film, but without the trapping of nanocrystals. In this control setup, the concentration of nanocrystals was raised by about 1800-fold to yield an emission spectrum akin to the one observed in the diluted solution using the trapping method.

The various DNH apertures used in this experiment were designed to be nominally identical, resulting in comparable emission intensities across different DNHs.

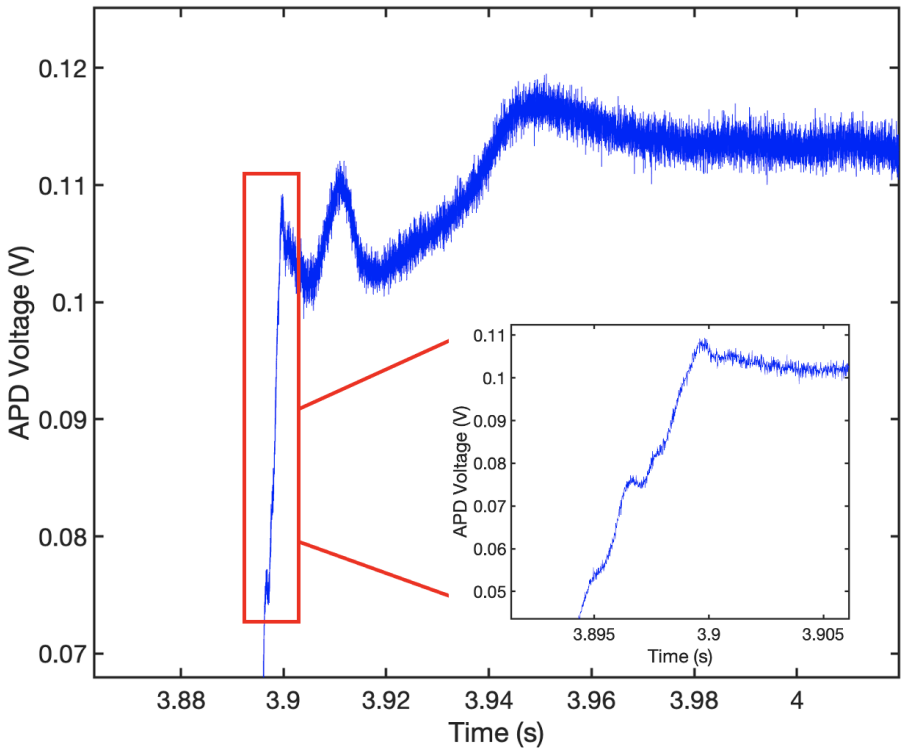

FIGURE 3.13: Trapping signal of a 20 nm $NaDyF_4$ nanoparticle in hexane. The inset shows the trapping moment.

3.2 Microdisk Fabrication using Er-doped silica Thin Film

3.2.1 Silica Thin Film Fabrication

In the framework of this research, the sol-gel method, a renowned technique for the synthesis of thin films, was employed for the fabrication of Er-doped silica films. The process commenced with the utilization of tetraethyl orthosilicate (TEOS) (99%) and isopropanol as the foundational precursor materials. To incorporate Er^{3+} ions into the silica matrix, $ErNO_3.5H_2O$ (99.9%) and hydrochloric acid (36.5%) were methodically used, targeting a precise Er weight concentration of 2%. All the materials were bought from Sigma-Aldrich.

The preparatory phase involved the dissolution of 0.2 g of $ErNO_3.5H_2O$ in 13 g of deionized water, forming the Er^{3+} solution. This solution, in the quantity of 1.3 g, was then introduced into a Pyrex beaker containing 12 g of isopropanol. Following this, 10 g of TEOS were added to the mixture, which was subsequently subjected to thorough stirring. The addition of 1 mL of hydrochloric acid was executed drop by drop, ensuring optimal integration within the mixture. The resultant solution was continuously stirred at a velocity of 450 rpm for a duration of 3 hours. This stirring process was conducted in an oil bath, maintained at a temperature of 68ºC, as depicted in Figure 3.14.

Upon completion of the stirring phase, the solution was allowed to age under ambient conditions for 24 hours, fostering the maturation of the sol-gel. The thin

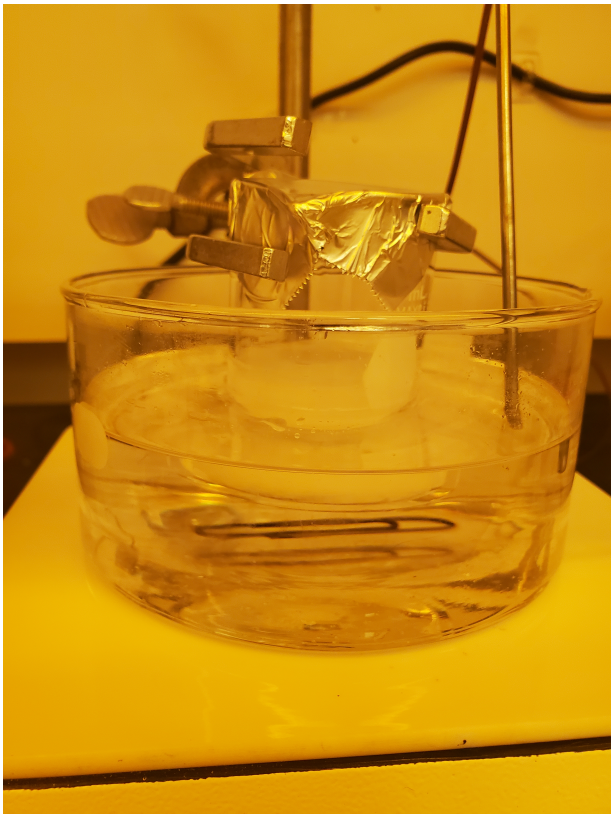

FIGURE 3.14: Sol-gel synthesis setup.

film fabrication involved depositing a layer of this sol-gel mixture onto a polished silicon (111) substrate via the spin coating technique. This crucial step entailed rotating the mixture at 3000 rpm for 30 seconds, thereby facilitating rapid solvent evaporation and the formation of a gel-like network through sol cross-linking.

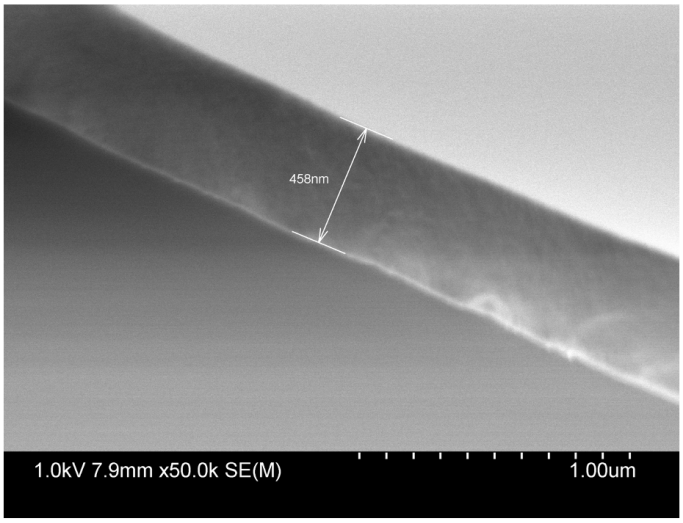

FIGURE 3.15: SEM picture of the first deposited layer of silica thin film.

Subsequent to the spin coating, the deposited film underwent an annealing process. This annealing, conducted in a tube furnace as shown in Figure 3.16, lasted for 3 hours at an elevated temperature of 1000°C, under ambient conditions. The primary objective of this annealing phase was to ensure the complete evaporation of any residual solvent, thereby converting the porous silica structure into a compact glass form. Following this high-temperature treatment, the wafer was allowed to cool naturally to ambient temperature. The resulting film had a thickness of ~ 500 nm. This was verified by measuring the thickness of the first deposited layer of thin film from SEM, as shown in Figure 3.15.

To achieve the targeted film thickness of approximately 1.5 µm, the processes of sol-gel deposition, spin coating, and annealing were meticulously repeated three times. The thickness of the final film was accurately determined using SEM, with

the results presented in Figure 3.17. This systematic approach facilitated the successful fabrication of erbium-doped silica thin films with precise control over their physical and chemical properties.

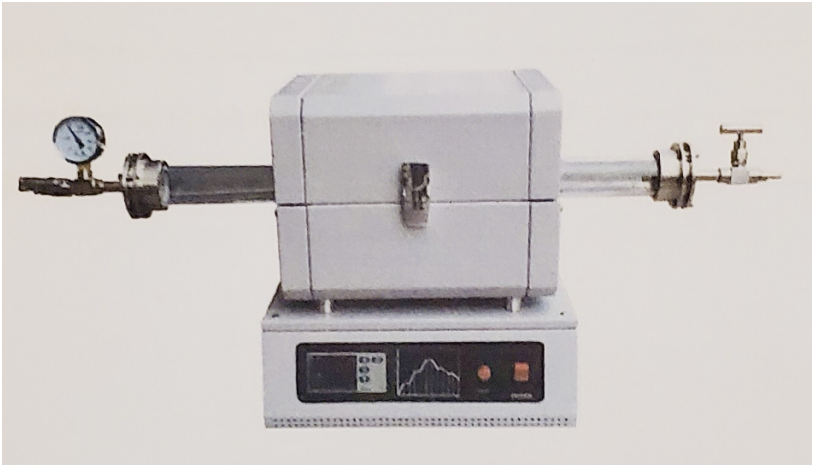

FIGURE 3.16: Tube furnace for annealing procedure.

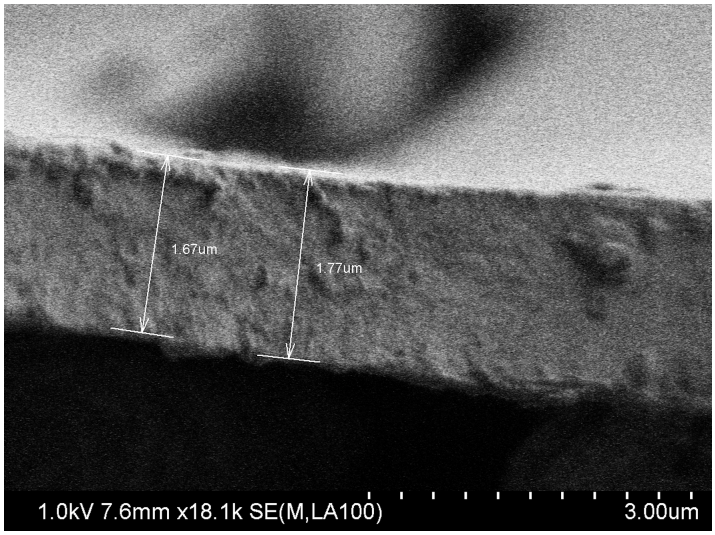

FIGURE 3.17: SEM picture of the final silica thin film.

3.2.2 Microdisk Fabrication

The fabrication procedure for silica circular pads, also called microdisks, involves a three-step process: deep UV photolithography, HF wet etch, and XeF_2 dry etch. These three steps are carefully controlled and optimized to achieve the desired shape and size of the microdisks.

The first step, deep UV photolithography, requires using a photosensitive material that is exposed to deep UV light through a mask with a desired pattern. This process transfers the pattern onto the photosensitive material, which is then developed to create a patterned resist layer. The resist layer functions as a protective layer for the substrate material during the wet etching process.

The second step, HF wet etch, is a chemical procedure that removes the unprotected silica substrate. The resist layer functions as a mask to protect the underlying silica material, which is then etched away using a hydrofluoric acid (HF) solution. This process creates the desired shape of the microdisk.

The final step, XeF_2 dry etch, removes the residual photoresist layer and refines the edges of the microdisk. XeF_2 gas is used to selectively etch away the remaining resist layer, leaving behind a clean and well-defined microdisk structure [114].

Photolithography

The silica-on-silicon wafer underwent a meticulous cleaning process and a subsequent drying phase at 150°C for 20 minutes to eliminate any contaminants that might impede the fabrication process. Once cleaned, a uniform layer of S1813, a

positive photoresist, was applied to the wafer using spin-coating techniques. The photoresist was then subjected to a pre-bake step at 115°C for one minute to attain the required hardness for the subsequent steps. To delineate the microdisk design onto the wafer, UV lithography was employed. The photomask, as seen in Figure 3.18, was strategically positioned over the wafer. When UV light was passed through the photomask, it selectively exposed the photoresist on the wafer to UV light. This exposure leveraged the pattern of opaque and transparent features on the photomask to create a corresponding pattern in the photoresist. The areas of the photoresist shielded by the opaque regions of the photomask remained unexposed and therefore soluble, whereas the exposed regions underwent a photochemical reaction, rendering them insoluble. The resulting pattern in the photoresist served as a negative of the microdisk design intended for the wafer, preparing it for the subsequent etching phases of the fabrication process. This step was performed using the deep UV photolithography system shown in Figure 3.19.

Following the 7-second UV exposure, the sample underwent a post-bake step for one minute at 115°C to ensure complete hardening of the photoresist and preservation of the pattern created by the UV exposure. The wafer was then immersed in a developer solution (MF-319) for one minute to remove the photoresist from areas of the wafer that had not been exposed to UV light, leaving only the microdisk design. Following a drying process (3 minutes at 115°C), the wafer was rinsed with DI water to remove any remaining traces of the developer solution. This completed the process of creating a silica-on-silicon wafer with a microdisk design using UV

lithography and a positive photoresist.

FIGURE 3.18: Photomask containing the designed microdisk pattern.

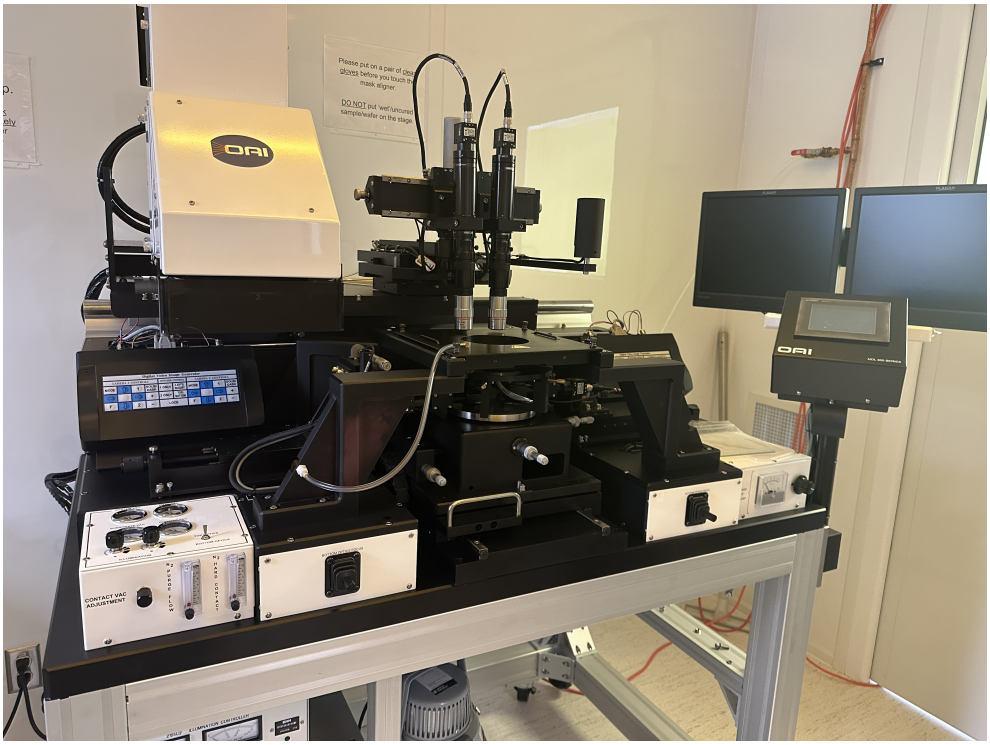

FIGURE 3.19: Deep UV photolithography system

Wet Etching

The described procedure entails the utilization of Buffered Hydrofluoric Acid (Transene) to selectively remove the silica from the surrounding area of microdisks. In order to perform this procedure, the wafer was immersed in Buffered HF for 20 minutes. This facilitated a chemical reaction with the silica, resulting in its removal from the surface of the microdisks. Then, the wafer went through a rinsing process utilizing deionized (DI) water. The next step in the process was to remove the photoresist from the top of the microdisks. To remove the photoresist, the wafer was sonicated in acetone for 15 minutes.

Dry Etching

The last two steps were done to create series of silica microdisks on a silicon wafer. After the formation of the microdisks, they were transferred to an etching chamber for further processing.

In this step, microdisks were subjected to an etching procedure using XeF_2 gas within the etching chamber. Each cycle, lasting 150 seconds, involved a sequence of actions where the chamber was first purged to ensure a contaminant-free environment. Subsequently, XeF_2 gas was introduced, which adsorbed onto the silicon surface of the microdisks. The ensuing chemical reaction selectively etched away the silicon, producing volatile byproducts that were then removed in the purging phase. This cycle repeated for several iterations (depending on the disk size and required pillar size), with each instance contributing to the gradual undercutting of the disks. The meticulous process effectively dissolved the silicon beneath the disks, enabling their suspension in the air, supported solely by strategically placed pillars. The isotropic nature of the XeF_2 etching facilitated a uniform removal of the material around the microdisks, ensuring their structural integrity and uniformity. This helps to isolate the resonator from the silicon substrate, reducing the interaction with the silicon and improving the Q factor. The microdisks' underlying silicon was selectively etched away by XeF_2 gas, resulting in the formation of the pillars. This stage is essential for obtaining microresonators with high Q, as it is necessary to reduce the interaction between light and silicon underneath the cavity to a minimum. However, there is a limit to how much the material can be

undercut, as excessive undercutting can lead to buckling. This buckling effect can lower the quality factor or, in some cases, cause the disk to fracture. During the etching cycles, the microdisks are subjected to forces that may lead to buckling, particularly after the underlying silicon is undercut. The isotropic etching action of XeF_2 can cause a uniform removal of silicon around the microdisks, creating a suspended structure supported by small pillars. If the intrinsic stresses from the deposition or etching process are not properly managed, or if there is a significant stress gradient due to temperature changes or uneven etch rates, these stresses can manifest as buckling once the structural support is compromised.

Furthermore, the aspect ratio of the microdisk to the supporting pillars plays a pivotal role. As the microdisk becomes thinner or the pillars longer, the capacity of these structures to withstand lateral forces diminishes, increasing the likelihood of buckling under the residual stresses or any external loads applied during subsequent processing steps. Additionally, the chemical reactions involved in the etching process may contribute to the stress within the microdisk material, leading to buckling, especially if the gaseous byproducts are not evenly dispersed.

3.2.3 Quality Factor Measurement

In the last part of the experiment, we focused on determining the intrinsic quality factors (Q) of microdisk resonators. To achieve this, we utilized a Newfocus TLB 6718-D external cavity tunable laser, operating at a wavelength of 970 nm. This choice of wavelength was instrumental in probing the resonators effectively. The

microdisks were meticulously probed with a tapered optical fiber, selected for its precision and efficiency in coupling light from the laser into the microdisk cavities.

Throughout the experiment, we carefully tuned the laser wavelength to align it with the microdisk cavity's resonance wavelength. This crucial step led to an important observation, as captured in Figure 3.20. We observed a Lorentzian-shaped signal in the transmission output recorded by the tapered fiber, indicative of a resonant interaction between the incoming light and the microdisk cavity.

On the oscilloscope, this resonant interaction was visualized in several waveforms:

The green sinusoidal waveform represents the modulated signal of the tunable laser, which is essential for tracking the response of the microdisk resonator. This modulation helps in identifying the resonance characteristics by creating a periodic signal that interacts with the microdisk. The blue waveform shows the transmission signal, which takes on a Lorentzian shape when resonance is achieved, signifying the efficient coupling of light into the microdisk cavity. The yellow waveform is the triangular signal representing the linear wavelength scan of the tunable laser, used to sweep across the resonance frequency.

By tuning the laser and observing these waveforms, particularly the green sinusoidal trace, we can determine the resonance characteristics and intrinsic quality factors of the microdisk resonators.

Our subsequent analysis focused on calculating the intrinsic Q factor of the microdisk resonators. This involved a comprehensive evaluation of the characteristics

FIGURE 3.20: Lorentzian-shaped signal in the output transmission detected by the tapered fiber shown oscilloscope screen.

of the Lorentzian signal, providing insights into the efficiency and energy retention properties of the microdisks.

Chapter 4

Result and Discussion

4.1 Thermometric Analysis of Nanoaperture Trapped Erbium Containing Nanocrystals

In this section, we present a detailed ratiometric analysis of the localized temperature increase within shaped nanoaperture optical tweezers, employing Er-doped nanocrystals as our primary sensing medium. This approach aligns with recent advancements in the field, as evidenced by other researchers who have successfully trapped Er-containing nanocrystals using innovatively shaped apertures to augment emission efficiency [115]. A notable advantage of utilizing upconverting particles in our temperature sensing methodology is their stable emission, which is crucial for long-term and reliable sensing applications. Unlike some conventional methods, our approach does not necessitate the use of dual laser sources—one for trapping and another for emission excitation. This singular source technique not only simplifies the experimental setup, but also enhances the overall efficiency

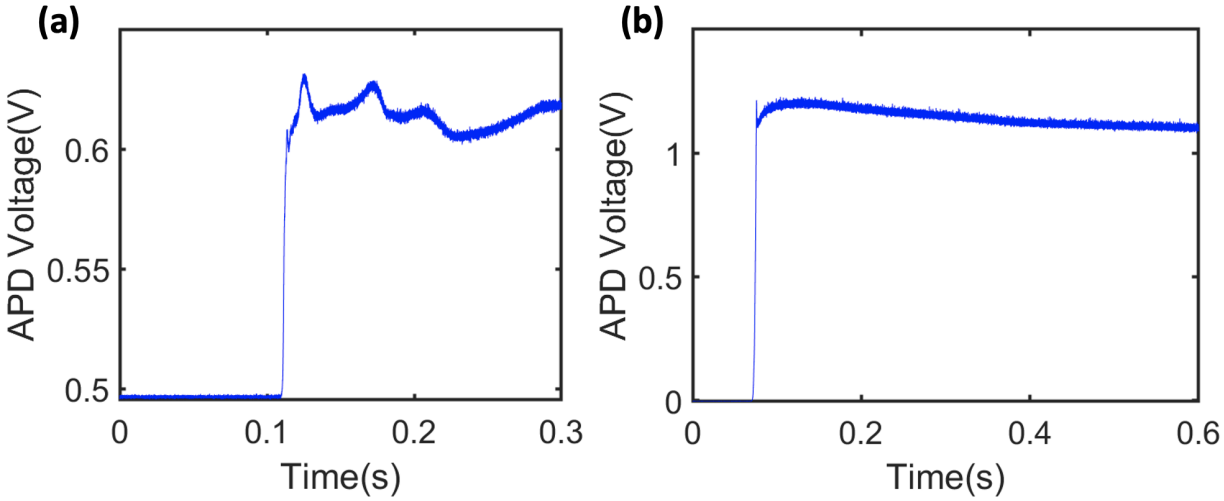

FIGURE 4.1: (a) Trapping signal of nanocrystals as measured as a voltage on APD, with oscillations after the laser is turned on (b) APD signal from hexane without nanocrystals when the laser is turned on. Adapted with permission from [116] © 2024, American Chemical Society

of the process. Furthermore, the plasmonic structures employed in our study are relatively simpler to fabricate compared to those that incorporate nanopores. This simplicity in design and fabrication underscores the practicality and potential for broader application of our nanoaperture-based temperature sensing approach. By combining ease of fabrication with the robustness of Er-doped upconverting nanoparticles, we have developed a system that offers both enhanced performance and operational simplicity, making it a valuable tool in the study of temperature effects at the nanoscale.

Figure 4.1 (a) displays the observed trapping signal of $NaYF_4$ nanocrystals in hexane within a DNH. This signal is captured through the APD-measured transmission across the aperture. A significant shift is noted in the transmission levels

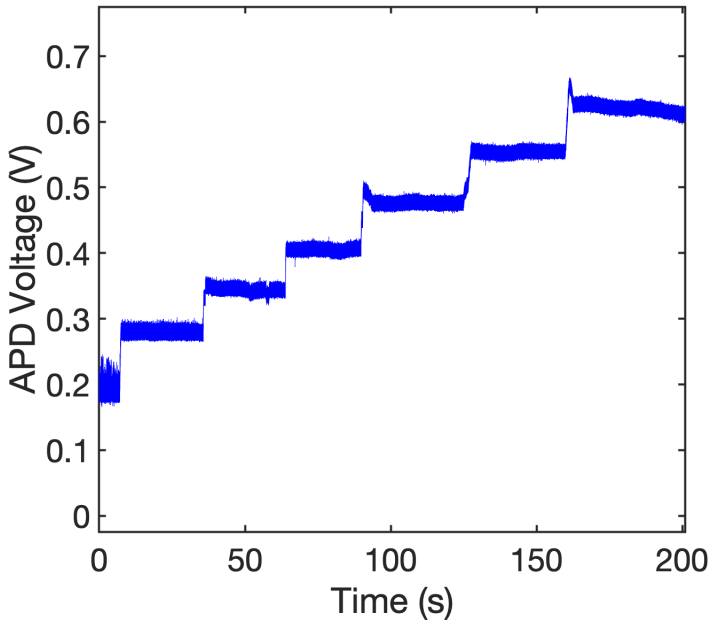

FIGURE 4.2: Intensity change of laser when acquiring spectra for a single trapped nanocrystal.

during the trapping event, with the disparity between the initial and final transmission levels, termed the 'jump height', being dependent on the particle's size and refractive index. For comparison purposes, Figure 4.1 (b) illustrates the baseline signal captured in the absence of particles when the laser is active.

Figure 4.5 demonstrates how the ratio of emission peaks at 527 nm and 542 nm is influenced by the power level for a 70 nm thick gold film post-trapping. For gold films of 100 nm and 130 nm thicknesses, similar data sets have been collected and are shown in Figure 4.6 (a) and (b).

Figure 4.7 (a), (b), and (c) depict the relationship between emission power and wavelength for a single trapped emitter in films with thicknesses of 70 nm, 100 nm, and 130 nm, respectively, displayed on a logarithmic scale. The observed slopes, which were near but slightly less than one, suggest that the system was functioning

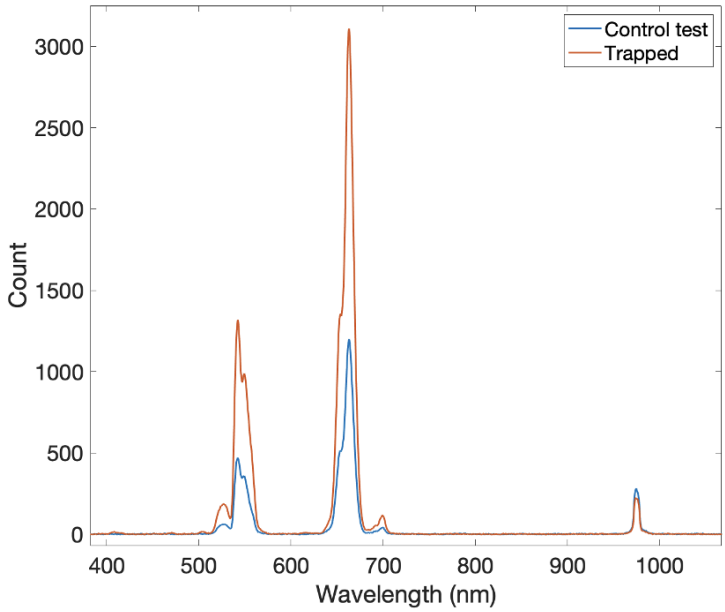

FIGURE 4.3: Comparison of emission spectra between the trapping of a nanocrystal from the diluted solution (1.3×10^{12} /mL), and the control experiment without any trapping with emission from the nanocrystals in bulk solution with concentration approximately 1800 times higher.

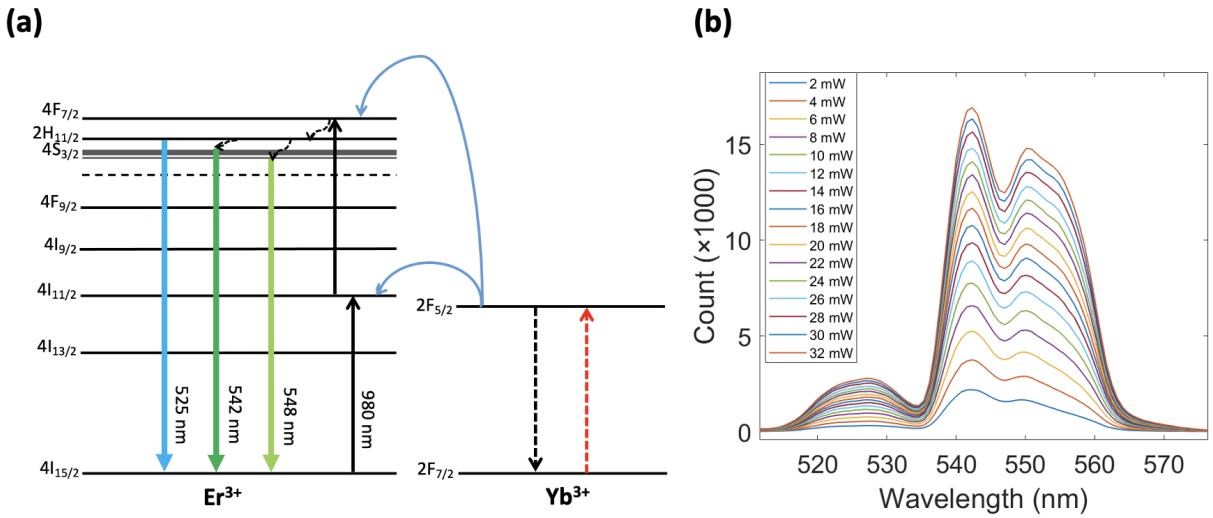

FIGURE 4.4: (a) Erbium energy level diagram and (b) Emission spectrum in different laser powers. Adapted with permission from [116]

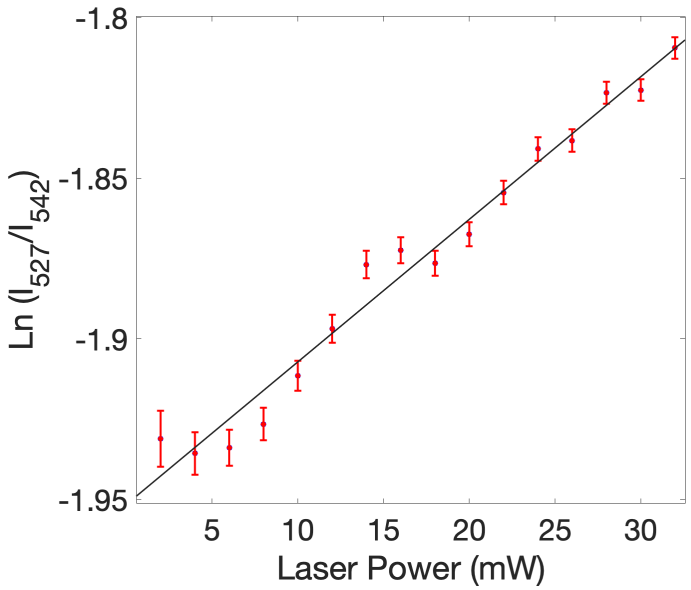

FIGURE 4.5: Power dependence of 527 nm and 542 nm emission peak ratio for 70 nm thick gold film. Adapted with permission from [116] © 2024, American Chemical Society

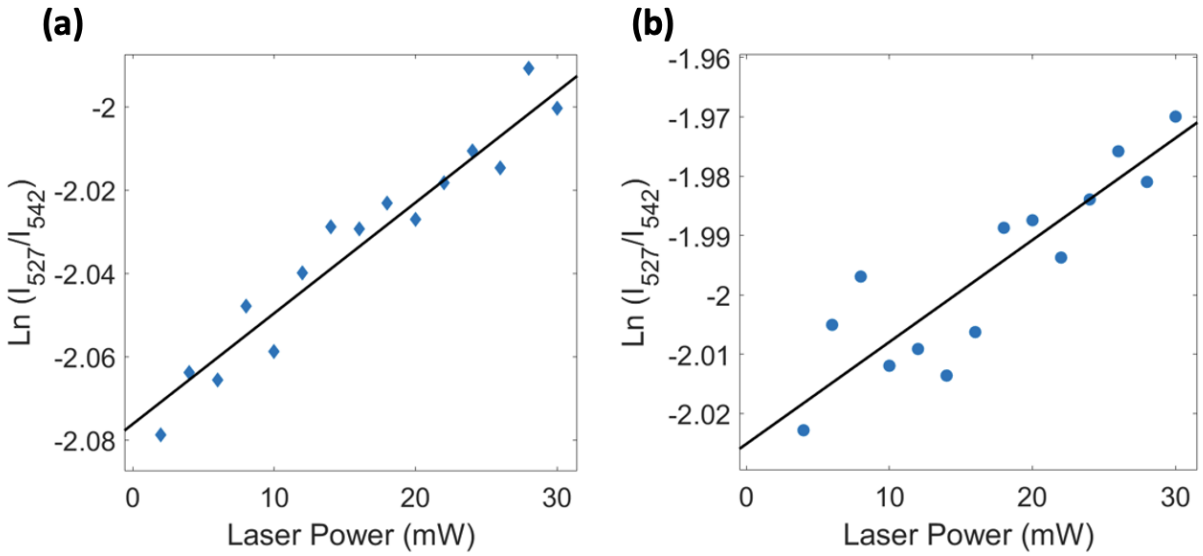

FIGURE 4.6: (a) Power dependence of 527 nm and 542 nm emission peak ratio for 100 nm thick gold film. (b) Power dependence of 527 nm and 542 nm emission peak ratio for 130 nm thick gold film.

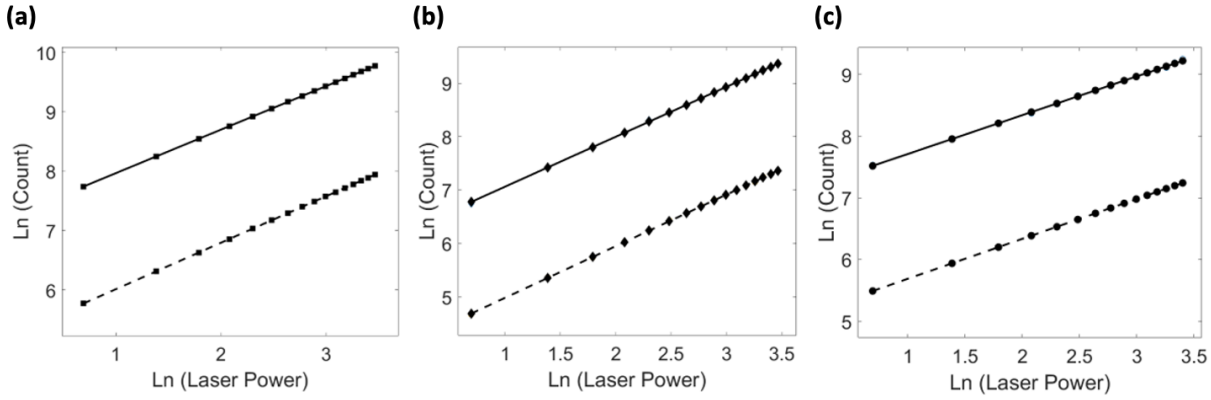

FIGURE 4.7: (a) Power dependence of the emission at 527 nm and 542 nm on a log-log scale for 70 nm thick gold film. (b) Power dependence of the emission at 527 nm and 542 nm on a log-log scale for 100 nm thick gold film. (c) Power dependence of the emission at 527 nm and 542 nm on a log-log scale for 130 nm thick gold film.

in a regime of intense excitation [117].

In exploring the intricacies of nanothermometry within our nanoaperture systems, we have identified the Boltzmann distribution as a key theoretical underpinning. This distribution allows us to understand the dependence of the emission intensity ratio on temperature and, by extension, on the laser pump power utilized within the system. Through careful measurements, we observed that the natural logarithm of the intensity ratio between emissions at wavelengths of 527 nm and 542 nm I_{527}/I_{542} displays a linear dependence on the applied power, providing a slope m, indicative of the temperature change per unit power:

$$\frac{dT}{dP} = -m\frac{kT_0^2}{\Delta E} \tag{4.1}$$

In this equation, ΔE denotes the energy difference between the two emission

states, k represents the Boltzmann constant, and T_0 is the ambient temperature, assumed here to be 293 K. This equation allows us to derive the rate at which temperature changes concerning the laser power, a critical parameter for the control and stability of temperature-sensitive processes within the nanoaperture.

To further dissect the relationship between emission intensities and temperature, we refer to the logarithmic expression of the Boltzmann distribution, which correlates the intensity ratio to the difference in energy levels and the absolute temperature:

$$\ln\left(\frac{I_1}{I_2}\right) = \ln\left(B\exp\left(-\frac{\Delta E}{kT}\right)\right) = \ln B - \frac{\Delta E}{kT} \tag{4.2}$$

where I_1 is the emission peak at wavelength (1), I_1 is the emission peak at wavelength (2), B is a constant depending on the emission rates, ΔE is the difference between two energy levels corresponding to these emissions, k is the Boltzmann constant and T is the temperature in Kelvin.

Differentiating this logarithmic ratio concerning power provides us with an expression for the slope in terms of the rate of temperature change with power:

$$\frac{d(\ln(I_1/I_2))}{dP} = \frac{\Delta E}{k\cdot T^2}\cdot\frac{dT}{dP} \tag{4.3}$$

These relationships become instrumental when considering the influence of the gold film's thermal properties on the system.

Previous research has explored the phenomenon where the local temperature

elevation is induced by a laser spot targeting a supported thin film. This temperature increase can be quantified as follows:

$$\Delta T = \frac{P_{\text{abs}}}{2\overline{\kappa} w_0 \sqrt{\pi}} \tag{4.4}$$

where the term κ represents the effective thermal conductivity, defined by the expression:

$$\overline{\kappa} = \kappa_s + 2\left(\frac{h_f}{w_0}\right)\kappa_f \tag{4.5}$$

Here, κ_s denotes the substrate's thermal conductivity, and κ_f is the film's thermal conductivity. The variable h_f refers to the film's thickness, and w_0 indicates the laser's $1/e^2$ spot size.

The role of absorbed optical power, P_{abs}, is pivotal in determining the resultant temperature elevation, and it is defined by the equation:

$$P_{\text{abs}} = P_0(1 - R - T) \tag{4.6}$$

where P_0 is the incident power of the laser. The variables R and T represent the film's reflectivity and transmissivity, respectively. Given that the film surpasses several skin depths in thickness, the transmissivity, T, is considered negligible, as discussed in the literature [118].

In an illustrative comparison shown in Figure 4.8, four distinct scenarios were

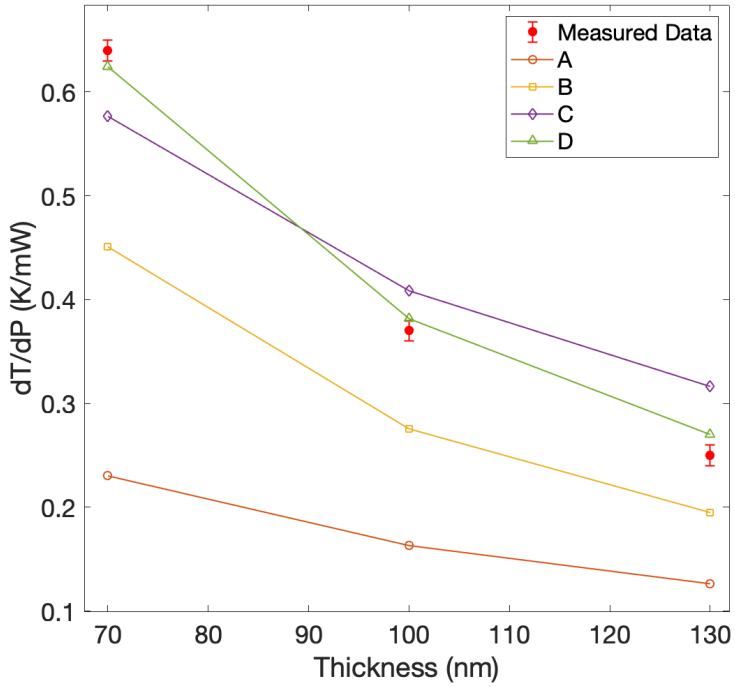

FIGURE 4.8: Power-dependent temperature change comparing experimental data (red filled circles) with the theory of Equation 4.4. A: Using the normal incidence Fresnel reflectivity and bulk thermal conductivity. B: Using the normal incidence Fresnel reflectivity and thickness-dependent thermal conductivity. C: Finding least squares fit to data with fitting parameter of reflectivity and using the bulk thermal conductivity. D: Finding least squares fit to data with fitting parameter of reflectivity and using the thickness-dependent thermal conductivity.

plotted against experimental data, revealing variations in temperature changes influenced by power. These scenarios considered the interplay between normal incidence Fresnel reflectivity and either bulk or thickness-dependent thermal conductivity. The process involved adjusting the aperture to measure a beam width of 1.34 microns through the transmission intensity profile.

The analysis extended to quantifying reflectivity and absorbed power alongside their impact on the root mean square error (RMSE) in each scenario. The highest

accuracy in fitting experimental data was achieved in Scenario D, which employed a thickness-dependent thermal conductivity model combined with adjusted reflectivity parameters. This scenario underscored the importance of considering variations in film thickness and its impact on thermal conductivity for accurate temperature prediction.

	R	$P_{\text{abs}} = P_0(1-R)$	RMSE
A	0.9718	0.0282	0.4754
B	0.9718	0.0282	0.2186
C	0.9294	0.0706	0.0996
D	0.9609	0.0391	0.0279
$W_0 = 1.34\,\mu\text{m}, P_0 = 1\,\text{mW}, n_{\text{hexane}} = 1.3749$ $n_{\text{gold}} = 0.21783 + 6.321i, K_s = 1.4\,\text{W}/(\text{m K})$			
Film Thickness (nm)		$K_f(\text{W}/(\text{m K}))$	
∞		317	
130 nm		203	
100 nm		184	
70 nm		155	

TABLE 4.1: Summary of values used in Figure 4.8.

The reflectivity values derived in Scenario D are deemed reasonable when considering factors such as surface roughness, gold quality, angle of incidence, and polarization, which can slightly alter this parameter. This analysis underlines the necessity of integrating thickness-dependent thermal conductivity to account for the observed dependencies in temperature elevation due to laser-induced heating on thin films. The graph shown in Figure 4.9 illustrates the variation of thermal conductivity in gold thin films as a function of their thickness. This scaling is essential because the thermal conductivity of a material in thin film form can differ

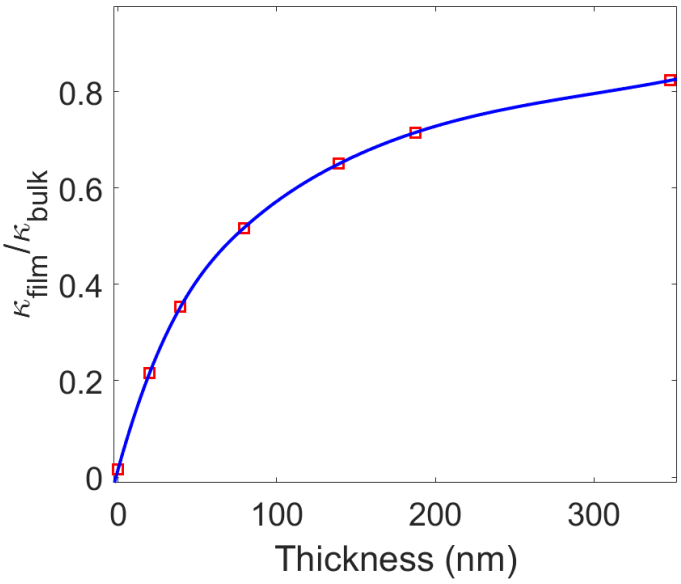

FIGURE 4.9: Scaled thermal conductivity of gold thin film in different thicknesses, digitally extracted from past work and fit with a local spline [119] .

significantly from its bulk counterpart because of the influence of surface scattering and grain boundary effects. As the thickness of the film decreases, these effects become more pronounced, often leading to a reduction in thermal conductivity.

Applying Equation 4.1 to our experimental findings, we determined the rate of temperature change concerning power (dT/dP) to be 0.64 K/mW for the 70 nm film, 0.37 K/mW for the 100 nm film, and 0.25 K/mW for the 130 nm film. In terms of noise analysis, the shot noise was the predominant factor, registering at least 44 counts for the weakest signal observed in Figure 4.4 (b). Other noise sources, such as dark noise, read-out noise, and shot noise on the dark current, were significantly lower, each being less than 3 counts as per the detector's specification sheet. This confirms that shot noise was the major contributor to the overall noise in our measurements.

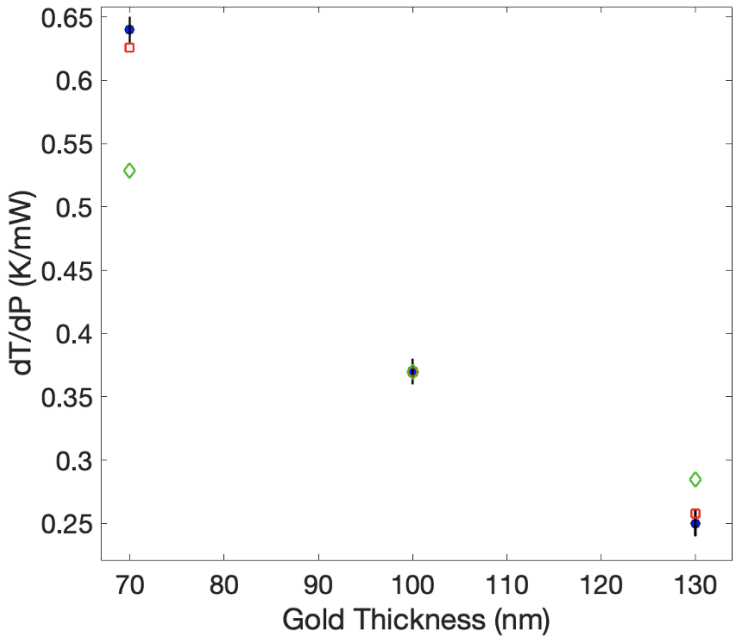

FIGURE 4.10: The caption describes the variation in temperature with power across different gold film thicknesses. Experimental results are depicted with blue circles, accompanied by error bars, while the basic theoretical prediction is represented by green diamonds. A more refined model, incorporating thickness-dependent thermal conductivity, illustrated with red squares, adjusts for variations in thermal conductivity as the film thickness changes [119]. To align the theoretical and experimental data, an adjustable scaling parameter was employed, specifically adjusted at a 100 nm thickness to match the experimental dT/dP value for that thickness. Subsequently, the same scaling factor was applied across other thickness measurements. Adapted with permission from [116] © 2024, American Chemical Society

Figure 4.10 presents the dependency of temperature change on the thickness of the material concerning pump power. Interestingly, the measured temperature changes significantly deviate from the simplistic expectation of an inverse relationship with thickness, an assumption that overlooks the impact of thickness-dependent thermal conductivity [119]. The key factor driving these variations in correlation with thickness is the dependence of thermal conductivity on the material's thickness. As thickness increases, thermal conductivity changes, impacting how temperature is distributed and how heat is transferred within the material, and consequently affecting the observed temperature gradient. The experimental results, particularly the correlation between thermal conductivity and gold thickness represented by red squares in the graph, align closely with theoretical calculations. This alignment is achieved after fitting the data with one of the points, thereby eliminating the need for a free scaling parameter. Moreover, the relatively small error margin, compared to the disparity between the measured values and the simplistic inverse dependency, underscores the importance of considering thickness-dependent conductivity in these analyses. Error bars shown in Figure 4.10 were derived using a range of slopes that could fit $\ln(I_{527}/I_{542})$ against laser power, as demonstrated in Figure 4.5 for the 70 nm thick gold film. This approach is referred to as the max-min slope method. The observation that thicker films exhibit lower temperature increases aligns with expectations, given that absorption predominantly occurs near the surface within the penetration depth, and

the gold effectively dissipates heat through thermal diffusion. Gold's thermal conductivity is noted to be 317 W/(m K) [120], while those for glass and hexane are approximately 1.4 W/(m K) and 0.13 W/(m K), respectively [121], [122]. The concept of skin depth, which refers to the depth at which light intensity decays and where most absorption occurs, is crucial in this context. The formula used for calculating the skin depth has been detailed in prior studies [123], [124]. For this specific wavelength, a skin depth (d) of 12 nm was determined using the relevant equations.

$$d = \frac{\lambda}{\mathrm{Im}\sqrt{\varepsilon_r} \times 4\pi} \tag{4.7}$$

where λ is the wavelength of the laser, ε_r is the relative permittivity of gold, and $\mathrm{Im}\sqrt{\varepsilon_r}$ is the imaginary part of the square root of the relative permittivity.

Previous studies on similar nanoaperture systems with 100 nm gold films have shown a temperature change of about 0.5 K/mW when the laser was directed from the gold side, not the adhesion layer side [67], [69], [125]. Notably, these reported values did not show significant variation depending on the shape of the aperture, the incident polarization, or the presence of a nanopore, indicating that the primary source of heating was the absorption by the gold film.

Figure 4.5 details how we have analyzed temperature changes with pump power in our study. The precision of our temperature measurements, established at 0.04 K/mW, and the accuracy, set at 2%, were ascertained through repeated trials and

by comparing our results to those anticipated from Equation 4.1. Earlier experiments employing different methods, like ion current in a nanopore, reported a temperature change of 0.48 K/mW [69], and studies using fluorescent particle tracking noted a change of 0.9 K μm^2/mW [66]. Another fluorescence spectroscopy study without trapping reported a significantly higher temperature change of 5 K μm^2/mW [67], exploring different fluorescence readouts such as intensity, diffusion time, and lifetime. A subsequent study by the same group found a temperature change with an intensity of 3 K μm^2/mW, investigating the effects of different nanoparticle surfactants on sensitivity [58]. In our work, we observed a temperature change of 0.37 K/mW for a 100 nm thick gold film, roughly half of what has been previously reported [68]. While the results are in the same general range, the discrepancy could be attributed to our experiments being conducted in hexane rather than water, which has a higher Thermo-optic coefficient, lower thermal conductivity, and a higher refractive index.

Our ratiometric sensitivity to temperature is about 20% lower than that reported in another study using a ratiometric method [126]. This discrepancy is likely because the energy peak difference we used is 20% smaller, and sensitivity scales with the ΔE value. One limitation of our method is the required thermal coupling of the rare-earth dopant energy levels. Another is the relative sensitivity linked to the ΔE value, where there's a balance to be struck: a higher ΔE increases sensitivity but reduces thermalization, lowering sensitivity [126]. When using higher ΔE luminescence intensity ratios for enhanced sensitivity, the population at the higher

excited level drops at lower temperatures, leading to decreased measurement resolution due to increased percentage uncertainty [127].

Our findings show temperature changes of 0.64 K/mW, 0.37 K/mW, and 0.25 K/mW for gold films of 70 nm, 100 nm, and 130 nm thickness, respectively. This indicates that thicker films significantly reduce local heating. Gold films' thermal conductivity on glass shows a thickness dependency in this range, linked to the grain boundary size and surface interactions [128]. To derive the theoretical scaling shown in Figure 4.10, we digitized data from a previous theoretical analysis on the thickness dependency of thermal conductivity [119] (Figure 4.9) and considered the inverse scaling of the heat source with film thickness. This approach, which assumes the temperature is roughly constant across the thin film and absorption is limited to the skin depth, aligns well with our experimental results. While we used the 100 nm thickness data for comparison, neglecting the thickness dependency of thermal conductivity does not offer as close a match for the 70 nm and 130 nm thicknesses.

In our experiments, we did not observe thermal convection effects at the attempted pump powers. Such effects were leveraged in previous studies to accelerate trapping in aqueous solutions, where the researchers used gold nanoislands within the aperture to increase local heating, potentially leading to bubble formation [56].

4.2 Assembly of Single-Photon Integrating Devices Using Photochemical Anchoring of Singly Er^{3+} Ion-Doped $NaYF_4$ Nanoparticles

A key focus of this experiment was to explore a photochemical approach for anchoring Er-doped nanocrystals inside DNH apertures. We investigated the possibility of optically trapping surface-functionalized nanocrystals in these nanoapertures, where they could anchor following a UV photo-triggered reaction. This novel method aimed to isolate a single Er emitter in a DNH for optimized emission.

$NaYF_4$ nanocrystals doped with trace amounts of Er^{3+} ions have been proposed as single-photon sources at 1550 nm. This hypothesis is based on the discovery of discrete intensity levels of Er^{3+}'s characteristic emissions in the visible region, which have been attributed to upconversion. Figure 4.11 (a) illustrates the discrete emission spectra of individual nanocrystals from 23 trapping events, captured within the 530 nm to 560 nm wavelength range, with an integration time of 1 second. The spectra exhibit distinct emission intensities, which are indicative of varying numbers of Er emitters present within each nanocrystal. These variations suggest the presence of discrete Er emitter counts within the nanocrystals, ranging from zero to four active emitters [129]. Through the integration of emission counts, it is possible to differentiate between nanocrystals containing different quantities of active Er emitters. Figure 4.11 (b) presents the probability distribution of the number of Er emitters per nanocrystal, both as anticipated from the synthesis (blue

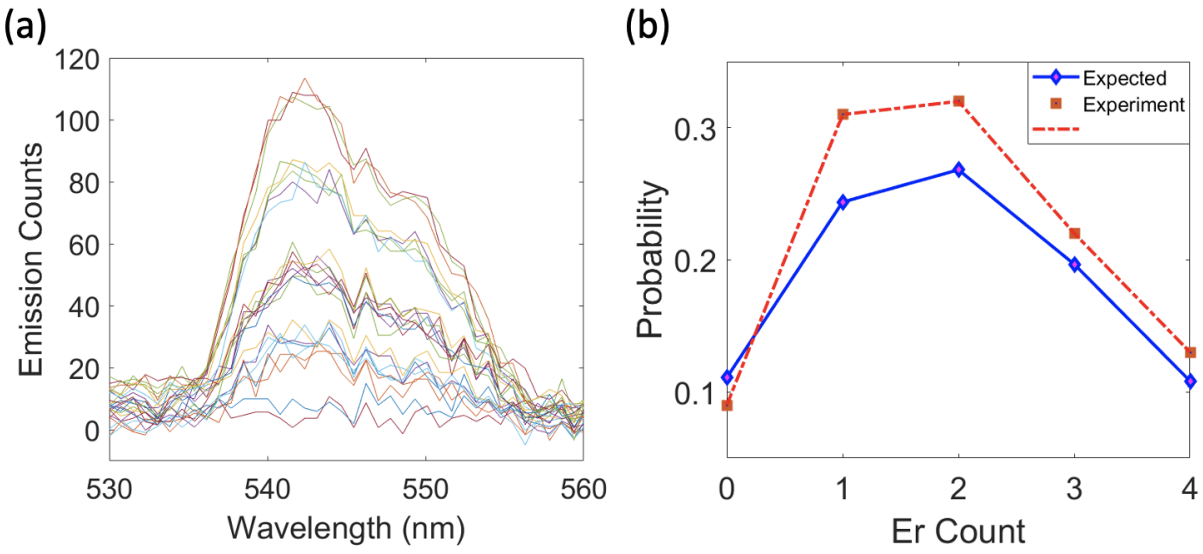

FIGURE 4.11: Discrete spectral intensity steps and Poisson distribution measured from the discrete intensity levels for samples with trace amounts of Er (on average 2.2 per particle)

line) and as observed in the experiment (red squares). This distribution presumes that every Er^{3+} ion is capable of photon emission. However, it is anticipated that surface quenching significantly diminishes the emission from Er^{3+} ions situated near the nanocrystal's surface. Quenching within a minimal surface layer could lead to a significant reduction in emission from a substantial fraction of the Er ions within the nanocrystal's volume. This level of quenching is a viable explanation, given the statistical uncertainties evident in the experimental outcomes.

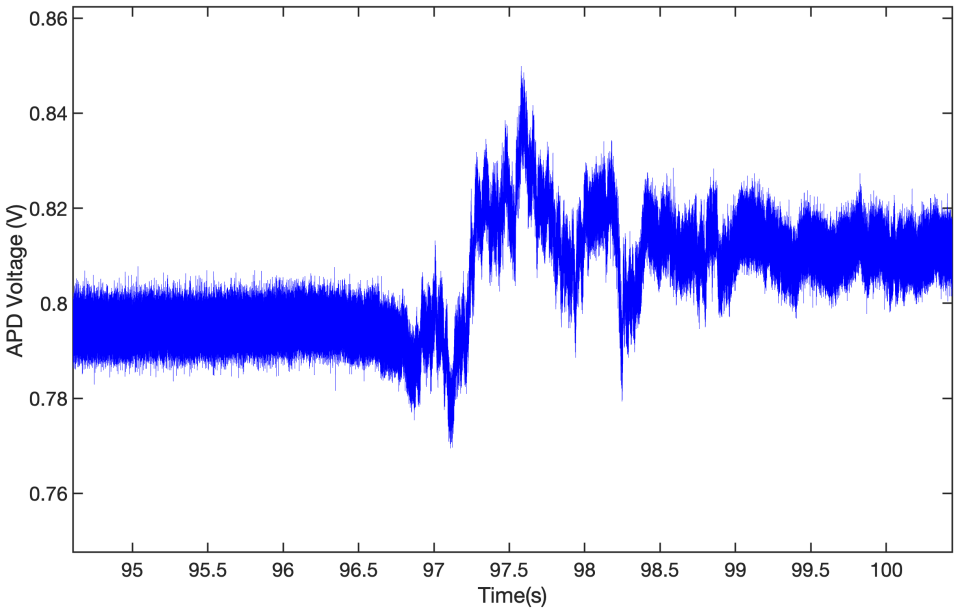

FIGURE 4.12: Trapping signal from low concentration Er-doped $NaYF_4$ nanocrystals in water measured by APD .

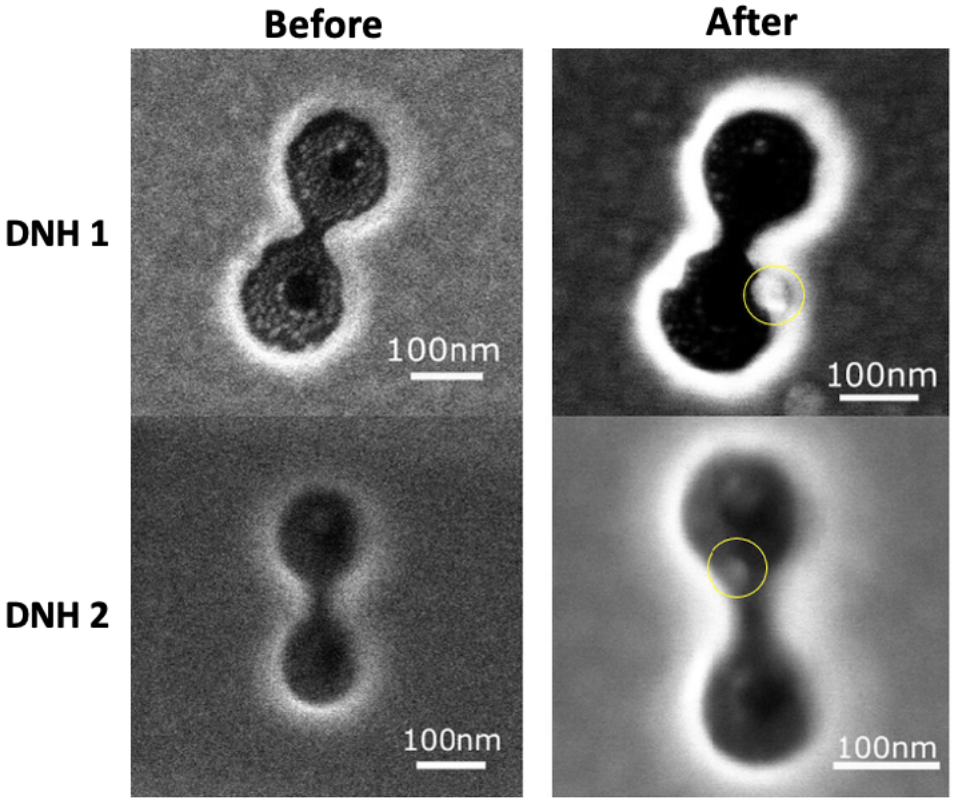

FIGURE 4.13: SEM image of DNHs before and after Er-doped nanocrystal attachment. Adapted with permission from [28] © 2023, American Chemical Society

4.3 Erbium-doped Microcavity Fabrication

4.3.1 Fabrication of Microdisk Resonators

The fabrication process began with the successful deposition of three layers of crack-free Er-doped silica thin films on silicon wafers, a critical step in ensuring the structural integrity and optical quality of the microdisks. The process, thoroughly outlined in the Experimental Method section, involved meticulous techniques to achieve uniformity and precision. The result of this deposition process is depicted in Figure 4.14, showcasing the layered structure of the films. In the pursuit of fabricating crack-free layers of thin film during each stage of the sol-gel process, one of the most significant challenges encountered was the prevention of cracks in the final silica film. The presence of cracks could severely compromise the integrity and functionality of the film as it has a direct and significant impact on the quality factor (Q) of the microdisk resonators fabricated from these thin films. The presence of cracks in the thin film can lead to scattering losses, which are detrimental to the optical properties of the microdisks. These scattering losses occur when light, confined within the microdisk resonator, encounters discontinuities in the material such as cracks. This interaction results in the dissipation of light energy out of the resonator, effectively reducing the Q factor. .To mitigate this problem, a rigorous approach was adopted, involving the careful monitoring and optimization of all parameters involved in the sol-gel synthesis and annealing steps. This included

precise control over factors such as precursor concentration, temperature, humidity, and curing time, ensuring that each layer of the thin film developed uniformly and without the formation of structural weaknesses. The success of this approach was pivotal in achieving the desired quality and consistency in the thin film, which is essential for its intended applications. This attention to detail in the fabrication process underscored the complexity and precision required for advanced material synthesis. Following the deposition, microdisk resonators were crafted utilizing the methods described earlier. The fabrication process was monitored and documented at various stages. Figure 4.16 (a) captures the appearance of a microdisk with a diameter of 120 µm post-photolithography, revealing the patterns created in the thin film. Subsequently, Figure 4.16 (b) illustrates the microdisk following the dry etching step which was performed in 90 cycles. The dry etching step was performed in 65, 90 and 110 cycles on different microdisks of the same diameter to achieve the optimum structure and Q factor. Notably, as evident in Figure 4.16 (b), a pillar structure formed beneath the disk. This feature, the centred circle, is crucial as it supports the disk and plays a significant role in the resonator's optical properties. An additional perspective is offered in Figure 4.17, which presents a side view of a fabricated microdisk with a diameter of 100 µm. This SEM image vividly shows the microdisk suspended in air, supported by the etched pillars. This striking visual confirmation underscores the success of the etching process, crucial for creating micro electromechanical systems (MEMS) that rely on such intricate and precise structural configurations.

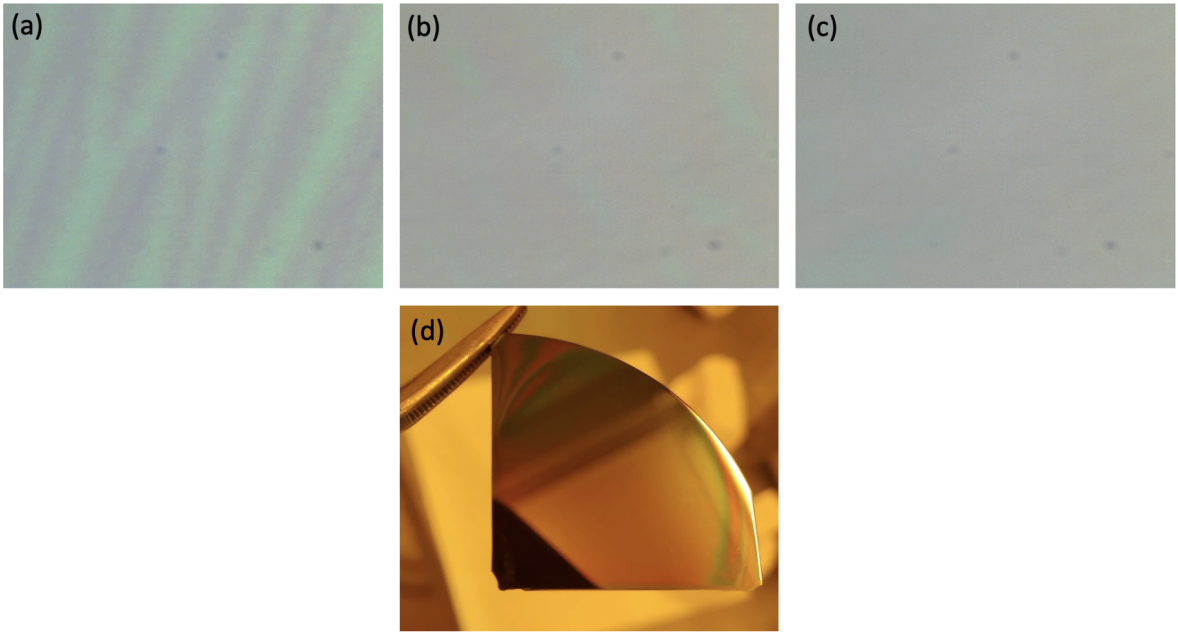

FIGURE 4.14: Microscope image of three layers of deposited Er-doped silica thin film after the annealing process. (a) The first layer, (b) The second layer (c) The third layer, and (d) The final thin film on a silicon wafer.

In Chapter 3, we encounter a pivotal challenge within the dry etching process: the propensity for buckling as we increase the number of etching cycles. This phenomenon, characterized by a deformation or warping of the structure, is a critical limitation when striving for minimal pillar sizes. Figure 4.15 presents a stark illustration of this issue, displaying a 120 µm microdisk that has succumbed to buckling after undergoing 110 cycles of dry etch. This instance highlights the delicate balance required in the etching process to maintain structural integrity and calls for meticulous optimization of the etching protocol.

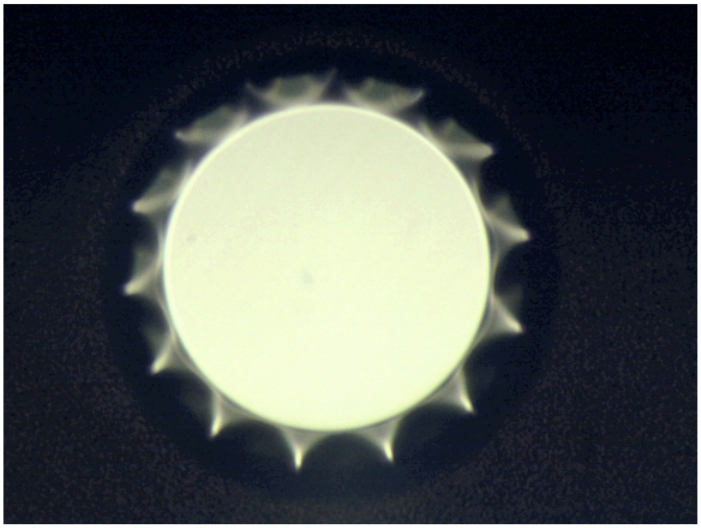

FIGURE 4.15: Microscopic image of 120 µm microdisk after 110 cycles of dry etching.

4.3.2 Measurement of Intrinsic Quality Factors

Turning our focus to the optical properties, we embarked on measuring the intrinsic or unloaded Q factor of these microdisk resonators. The method is described in the Experimental Method section. The microdisks were probed using a tapered optical fiber, a technique chosen for its ability to enable precise and efficient light coupling from the laser into the microdisk cavities. This method of probing is pivotal as it ensures minimal loss and maximum interaction between the light and the resonator, which is crucial for accurate Q factor measurements. These measurements are fundamental in understanding the efficiency and performance of the microdisk resonators. The Q factor, a key parameter in resonator physics, indicates the resonator's ability to confine light and is indicative of the energy loss relative to the stored energy within the resonator. Higher Q factors signify lower energy

loss and are desirable in various applications, including in optical communications and sensing technologies. The successful fabrication of these microdisk resonators, coupled with the precise measurement of their intrinsic Q factors, marks a significant achievement in our research. It not only demonstrates our capability to create structurally sound and functionally effective microdisks but also paves the way for further exploration into their potential applications in advanced optical systems.

During the experiment, we meticulously adjusted the laser wavelength to match the resonance wavelength of the microdisk cavity, leading to a notable finding depicted in Figure 3.20. We detected a Lorentzian-shaped transmission signal via the tapered fiber, signaling a resonant interaction between the laser light and the microdisk cavity.

Central to this analysis was the concept of the Q factor, which is fundamentally linked to the resonance peak's sharpness. In more technical terms, the Q factor is defined as the ratio of the resonant frequency (alternatively, the resonant wavelength) to the bandwidth of the resonance. This bandwidth is quantified as the full width at half maximum (FWHM) of the Lorentzian peak. This relationship signifies that a higher Q factor corresponds to a narrower FWHM, indicating a more efficient and precise resonant interaction within the microdisk cavity. This correlation between the Q factor and the sharpness of the resonance peak is crucial as it directly influences the performance and potential applications of the microdisk resonators. A higher Q factor denotes lower energy loss within the cavity, translating to better performance in applications such as optical filters, sensors, and lasers.

The methodology and results from this analysis not only contribute to our understanding of the resonant properties of microdisk cavities but also open avenues for optimizing and tailoring these devices for specific technological applications.

$$Q = \frac{f}{\Delta f} \tag{4.8}$$

In the wavelength domain, this equation translates to:

$$Q = \frac{\lambda_{\text{resonance}}}{\Delta\lambda_{\text{FWHM}}} \tag{4.9}$$

Using the oscilloscope, we meticulously measured the width of the Lorentzian dip, a critical step in determining $\Delta\lambda_{\text{FWHM}}$, which is the full width at half maximum of the resonance. The resonance wavelength, denoted as $\lambda_{\text{resonance}}$, was accurately known from the tuning range of the laser we employed. Equipped with these crucial measurements, we were able to calculate the Q factor of 6.7×10^6 for the microdisk resonator which underwent 90 cycles of dry etching. This high Q factor is indicative of an exceptionally sharp resonance peak and correspondingly, a very narrow FWHM. The experimental process detailed in the Experimental Method chapter elucidates that the efficiency and Q of a microresonator are significantly influenced by the extent of its contact with the underlying silicon substrate. A smaller contact area is synonymous with a higher Q due to reduced energy dissipation. This principle is exemplified in the case of a microdisk, dry etched for 65 cycles as depicted in Figure 4.18, which exhibited a Q of 8×10^5. This value aligns

with our expectations; the microdisk with a larger pillar, indicative of less etching and thus a broader contact base, naturally possesses a lower Q in comparison to a counterpart with a reduced contact area. The observed correlation between the contact size and the resonator's Q not only reinforces our understanding of the microdisk's vibrational dynamics, but also serves as a guidepost for refining etching protocols to optimize resonator performance. The oscilloscope's detailed readouts, including the specific markers for time and voltage, were instrumental in enabling us to determine these values with high precision. The characteristics of the dip observed in the waveform–its sharpness and exact position on the oscilloscope display–were key to accurately calculating the Q factor. This calculation is not just a numerical exercise but provides profound insights into how effectively the microdisk resonator can store energy and the extent of energy loss at the operational wavelength of 970 nm. The significance of a high Q factor cannot be overstated. It reflects the resonator's capacity to maintain energy within it for a longer period before that energy dissipates. In practical applications, such a high Q factor translates to enhanced performance in areas like sensing, telecommunications, and photonics, where energy efficiency and precision are paramount. The methodology we employed and the results we obtained thus mark a significant advancement in the field of microdisk resonator technology, showcasing the potential of these systems in cutting-edge optical applications.

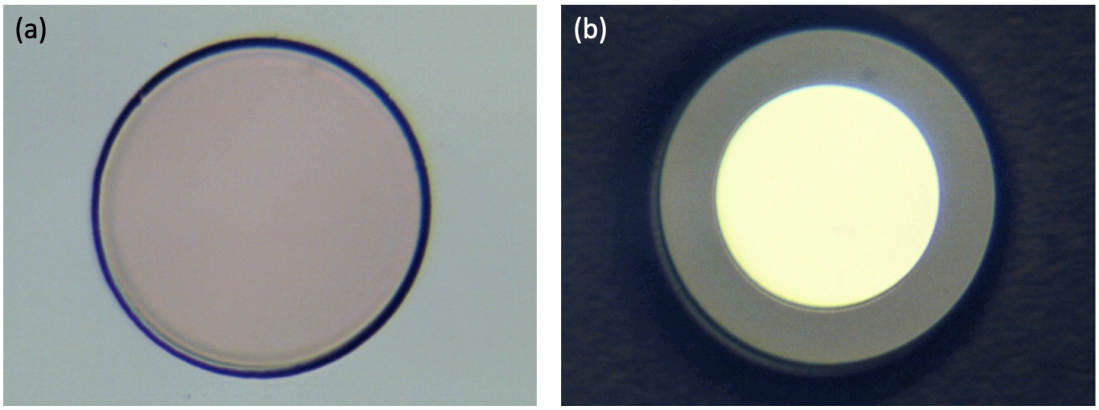

FIGURE 4.16: Microscopic image of 120 µm microdisk (a) after photolithography step, and (b) after dry etching step (90 cycles).

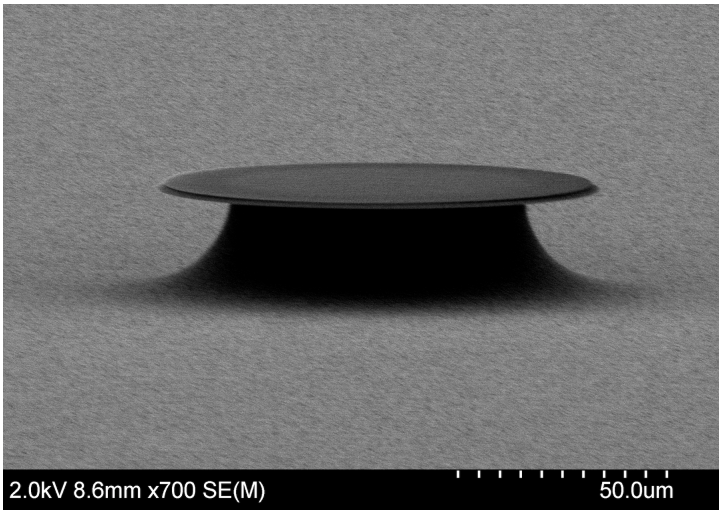

FIGURE 4.17: SEM image of 120 µm fabricated microdisk.

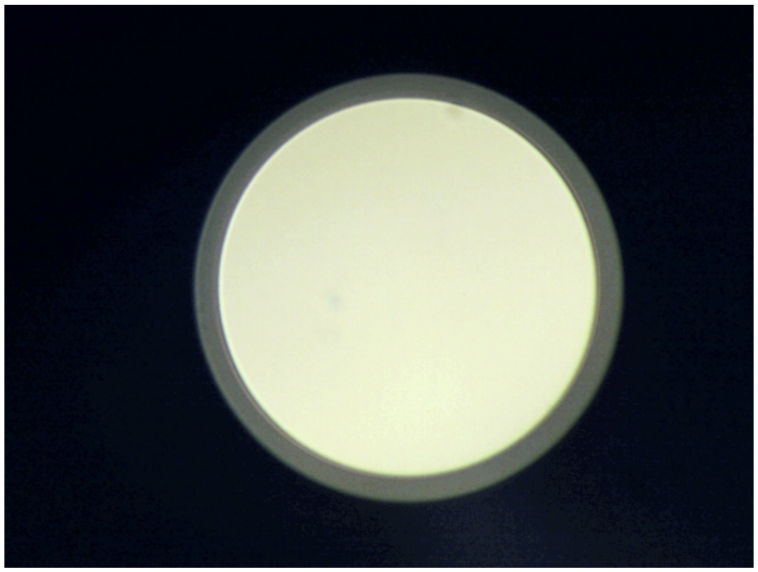

FIGURE 4.18: Microscopic image of 120 µm microdisk after 65 cycles of dry etching.

Chapter 5

Conclusion

This dissertation has made crucial advancements in nanothermometry and optical resonator technology, focusing especially on the innovative integration of single-photon sources within double nanoholes. These contributions mark significant progress in the realms of photonics, quantum optics, and nanotechnology.

5.1 Nanothermometry

A significant portion of this research was dedicated to the exploration and understanding of nanothermometry. This work delved into the intricate details of how temperature changes at the nanoscale, especially concerning the power and thickness of gold films. By meticulously analyzing the thickness-dependent thermal conductivity of these films, the research has shed light on the critical aspects of thermal behaviour in nanostructures. The findings from these studies are not just academically intriguing; they hold immense practical value in the development of nano-devices where precise thermal management is vital. The ability to accurately

measure and control temperature at such a small scale opens up new possibilities in various applications, ranging from electronic devices to nanoscale chemical reactions.

This exploration of nanothermometry has provided a more profound understanding of heat transfer and temperature distribution at the nanoscale. It is a significant step towards optimizing the thermal properties of materials used in nanotechnology. It could lead to the development of more efficient thermal management systems in micro- and nano-electronics.

5.2 Microdisk Resonators

The fabrication of Er-doped silica microdisk resonators was another cornerstone of this dissertation. The journey from the deposition of crackless thin films to the creation of high-quality microdisk resonators demonstrated not only technical proficiency but also an advanced understanding of material properties and optical behaviour. The resonators' high intrinsic quality factors underscore their efficiency in light confinement and minimal energy loss. This is crucial for their potential applications in optical sensing, telecommunications, and laser technologies.

These microdisk resonators represent a significant advancement in resonator technology, offering new opportunities for enhancing the performance of optical devices. Their ability to maintain high Q factors is indicative of their potential to revolutionize the field of photonics, providing a platform for more efficient and precise optical systems.

5.3 Integration of Single-Photon Sources in DNH

The innovative work on integrating single-photon sources within double nanoholes demonstrates a unique intersection of nanofabrication techniques and quantum optics. This integration is a breakthrough in manipulating and controlling single-photon emissions, which is fundamental for the advancement of quantum computing and secure communication technologies. The successful attachment of these single-photon sources within double nanoholes not only validates the feasibility of such integrations but also opens the door to exploring more complex quantum systems.

5.4 Key Findings and Future Directions

The key findings from this dissertation include:

Advancements in Microdisk Resonator Technology: Highlighting the successful fabrication of high-Q microdisk resonators. Innovations in Nanothermometry: Enhancing our understanding of nanoscale thermal properties. Integration of Single-Photon Sources in Double Nanoholes: Pioneering work in quantum optics by effectively integrating single-photon sources within double nanoholes. Future research could explore further integration of these components — microdisk resonators and single-photon sources within double nanoholes — for advanced quantum technology applications. Additional studies could also delve into new materials and methods in both nanothermometry and quantum optics.

Conclusion In summary, this dissertation has contributed significantly to our understanding of nanothermometry, the development of microdisk resonators, and the integration of single-photon sources within double nanoholes. The research presented herein lays a robust foundation for future explorations and potential breakthroughs in photonics, quantum optics, and nanotechnology. The methodologies developed and the insights gained from this study pave the way for new research directions in these dynamic and rapidly evolving fields.

Bibliography

[1] D. Shahrjerdi, A. D. Franklin, S. Oida, J. A. Ott, G. S. Tulevski, and W. Haensch, "High-performance air-stable n-type carbon nanotube transistors with erbium contacts," *ACS Nano*, vol. 7, no. 9, pp. 8303–8308, 2013.

[2] T. F. Schulze and T. W. Schmidt, "Photochemical upconversion: Present status and prospects for its application to solar energy conversion," *Energy & Environmental Science*, vol. 8, no. 1, pp. 103–125, 2015.

[3] F. Wang, X.-Y. Yang, M.-s. Niu, *et al.*, "Enhancing light harvesting and charge transport in organic solar cells via integrating lanthanide-doped upconversation materials," *Journal of Physics D: Applied Physics*, vol. 51, no. 26, p. 265 105, 2018.

[4] A. Alizadehkhaledi, A. L. Frencken, F. C. van Veggel, and R. Gordon, "Isolating nanocrystals with an individual erbium emitter: A route to a stable single-photon source at 1550 nm wavelength," *Nano Letters*, vol. 20, no. 2, pp. 1018–1022, 2019.

[5] Q. Jiang, P. Roy, J.-B. Claude, and J. Wenger, "Single photon source from a nanoantenna-trapped single quantum dot," *Nano Letters*, vol. 21, no. 16, pp. 7030–7036, 2021.

[6] E. Saglamyurek, J. Jin, V. B. Verma, *et al.*, "Quantum storage of entangled telecom-wavelength photons in an erbium-doped optical fibre," *Nature Photonics*, vol. 9, no. 2, pp. 83–87, 2015.

[7] J. Zhou, Q. Liu, W. Feng, Y. Sun, and F. Li, "Upconversion luminescent materials: Advances and applications," *Chemical Reviews*, vol. 115, no. 1, pp. 395–465, 2015.

[8] B. Wang, P. Zhou, and X. Wang, "Recent progress in on-chip erbium-based light sources," *Applied Sciences*, vol. 12, no. 22, p. 11 712, 2022.

[9] T. M. Benson, S. V. Boriskina, P. Sewell, A. Vukovic, S. C. Greedy, and A. I. Nosich, "Micro-optical resonators for microlasers and integrated optoelectronics," in *Frontiers in Planar Lightwave Circuit Technology: Design, Simulation, and Fabrication*, Springer, 2006, pp. 39–70.

[10] E. F. Perez, G. Moille, X. Lu, J. Stone, F. Zhou, and K. Srinivasan, "High-performance kerr microresonator optical parametric oscillator on a silicon chip," *Nature Communications*, vol. 14, no. 1, p. 242, 2023.

[11] Y. Yang, Z. Wang, X. Zhang, Q. Zhang, and T. Wang, "Recent progress of in-fiber wgm microsphere resonator," *Frontiers of Optoelectronics*, vol. 16, no. 1, p. 10, 2023.

[12] S Berneschi, F Cosi, D Farnesi, *et al.*, "Glass based microresonators," in *Fiber Lasers and Glass Photonics: Materials through Applications*, SPIE, vol. 10683, 2018, pp. 75–82.

[13] A. Rasoloniaina, V. Huet, T. K. N. Nguyen, *et al.*, "Controling the coupling properties of active ultrahigh-q wgm microcavities from undercoupling to selective amplification," *Scientific Reports*, vol. 4, no. 1, p. 4023, 2014.

[14] Y. Liu, Z. Qiu, X. Ji, *et al.*, "A photonic integrated circuit–based erbium-doped amplifier," *Science*, vol. 376, no. 6599, pp. 1309–1313, 2022.

[15] G. Kucsko, P. C. Maurer, N. Y. Yao, *et al.*, "Nanometre-scale thermometry in a living cell," *Nature*, vol. 500, no. 7460, pp. 54–58, 2013.

[16] C. Bradac, S. F. Lim, H.-C. Chang, and I. Aharonovich, "Optical nanoscale thermometry: From fundamental mechanisms to emerging practical applications," *Advanced Optical Materials*, vol. 8, no. 15, p. 2 000 183, 2020.

[17] Z. Rao, Q. Li, Z. Li, L. Zhou, X. Zhao, and X. Gong, "Ultra-high-sensitive temperature sensing based on er3+ and yb3+ co-doped lead-free double perovskite microcrystals," *The Journal of Physical Chemistry Letters*, vol. 13, no. 16, pp. 3623–3630, 2022.

[18] Y. Zhao, X. Wang, R. Hu, and Y. Li, "Linear red/green ratiometric thermometry of ho 3+/cr 3+ co-doped red up-conversion tungstate materials," *Dalton Transactions*, vol. 50, no. 43, pp. 15 821–15 830, 2021.

[19] B. Hu, H. Zhang, L. He, and D. Wang, "Upconversion luminescence and temperature sensing properties of er3+/yb3+-doped α-binbo4 phosphor," *Journal of Electronic Materials*, vol. 52, no. 5, pp. 3386–3393, 2023.

[20] L. Yan, J. Huang, Z. An, Q. Zhang, and B. Zhou, "Activating ultrahigh thermoresponsive upconversion in an erbium sublattice for nanothermometry and information security," *Nano Letters*, vol. 22, no. 17, pp. 7042–7048, 2022.

[21] M. Di Giancamillo, P. Biagioni, V. Sorianello, and E. Prati, "Design of erbium doped silicon nanocavities for single photon applications," in *EPJ Web of Conferences*, EDP Sciences, vol. 255, 2021, p. 04 001.

[22] R. Gordon, "Biosensing with nanoaperture optical tweezers," *Optics & Laser Technology*, vol. 109, pp. 328–335, 2019.

[23] A. Laucht, F. Hohls, N. Ubbelohde, *et al.*, "Roadmap on quantum nanotechnologies," *Nanotechnology*, vol. 32, no. 16, p. 162 003, 2021.

[24] M. D. Birowosuto, H. Sumikura, S. Matsuo, *et al.*, "Fast purcell-enhanced single photon source in 1,550-nm telecom band from a resonant quantum dot-cavity coupling," *Scientific reports*, vol. 2, no. 1, pp. 1–5, 2012.

[25] T. Zhong, J. M. Kindem, J. G. Bartholomew, *et al.*, "Optically addressing single rare-earth ions in a nanophotonic cavity," *Physical review letters*, vol. 121, no. 18, p. 183 603, 2018.

[26] A. Dibos, M. Raha, C. Phenicie, and J. D. Thompson, "Atomic source of single photons in the telecom band," *Physical review letters*, vol. 120, no. 24, p. 243 601, 2018.

[27] Y. Pang and R. Gordon, "Optical trapping of 12 nm dielectric spheres using double-nanoholes in a gold film," *Nano letters*, vol. 11, no. 9, pp. 3763–3767, 2011.

[28] A. L. Frencken, M. Dobinson, Z. Sharifi, E. H. Toodeshki, R. Gordon, and F. C. J. M. van Veggel, "Photochemical anchoring of singly er^{3+} ion-doped $nayf_4$ nanoparticles for scalable fabrication of single-photon emitting devices: Implications for quantum light sources in the telecom window," *ACS Applied Nano Materials*, 2023.

[29] X.-F. Liu, F. Lei, T.-J. Wang, G.-L. Long, and C. Wang, "Gain lifetime characterization through time-resolved stimulated emission in a whispering-gallery mode microresonator," *Nanophotonics*, vol. 8, no. 1, pp. 127–134, 2018.

[30] W. Jin, Q.-F. Yang, L. Chang, *et al.*, "Hertz-linewidth semiconductor lasers using cmos-ready ultra-high-q microresonators," *Nature Photonics*, vol. 15, no. 5, pp. 346–353, 2021.

[31] N. M. Kondratiev, V. E. Lobanov, A. E. Shitikov, *et al.*, "Recent advances in laser self-injection locking to high-q microresonators," *Frontiers of Physics*, vol. 18, no. 2, p. 21 305, 2023.

[32] D. Woods, S. Sharifi, J. Melia, G. Bahl, and E. Goldschmidt, "Towards raman cooling in erbium doped microresonators," in *APS March Meeting Abstracts*, vol. 2022, 2022, G00–333.

[33] V. Braginsky, M. Gorodetsky, and V. Ilchenko, "Quality-factor and nonlinear properties of optical whispering-gallery modes," *Physics letters A*, vol. 137, no. 7-8, pp. 393–397, 1989.

[34] F. Vollmer, S. Arnold, D. Braun, I. Teraoka, and A. Libchaber, "Multiplexed dna quantification by spectroscopic shift of two microsphere cavities," *Biophysical journal*, vol. 85, no. 3, pp. 1974–1979, 2003.

[35] X.-F. Liu, T.-J. Wang, and C. Wang, "Optothermal control of gains in erbium-doped whispering-gallery microresonators," *Optics letters*, vol. 43, no. 2, pp. 326–329, 2018.

[36] G. Lin and Y. K. Chembo, "Monolithic total internal reflection resonators for applications in photonics," *Optical Materials: X*, vol. 2, p. 100 017, 2019.

[37] J. Yan, D. Wang, and X. Li, "An erbium-doped whispering-gallery-mode microlaser for sensing," *Journal of Lightwave Technology*, vol. 39, no. 15, pp. 5177–5182, 2021.

[38] X.-F. Liu, F. Lei, M. Gao, *et al.*, "Gain competition induced mode evolution and resonance control in erbium-doped whispering-gallery microresonators," *Optics Express*, vol. 24, no. 9, pp. 9550–9560, 2016.

[39] G. P. Agrawal, *Fiber-optic communication systems*. John Wiley & Sons, 2012.

[40] H.-B. Lin and A. Campillo, "Microcavity enhanced raman gain," *Optics communications*, vol. 133, no. 1-6, pp. 287–292, 1997.

[41] M. Cai, O Painter, K. Vahala, and P. Sercel, "Fiber-coupled microsphere laser," *Optics letters*, vol. 25, no. 19, pp. 1430–1432, 2000.

[42] A. Ashkin, J. M. Dziedzic, J. E. Bjorkholm, and S. Chu, "Observation of a single-beam gradient force optical trap for dielectric particles," *Optics letters*, vol. 11, no. 5, pp. 288–290, 1986.

[43] L. Huang and O. J. F. Martin, "Reversal of the optical force in a plasmonic trap," *Optics Letters*, vol. 33, no. 24, p. 3001, Dec. 2008.

[44] L. Novotny, R. X. Bian, and X. S. Xie, "Theory of Nanometric Optical Tweezers," *Physical Review Letters*, vol. 79, no. 4, pp. 645–648, Jul. 1997.

[45] M. Righini, P. Ghenuche, S. Cherukulappurath, V. Myroshnychenko, F. J. García de Abajo, and R. Quidant, "Nano-optical Trapping of Rayleigh Particles and Escherichia coli Bacteria with Resonant Optical Antennas," *Nano Letters*, vol. 9, no. 10, pp. 3387–3391, Oct. 2009.

[46] M. L. Juan, R. Gordon, Y. Pang, F. Eftekhari, and R. Quidant, "Self-induced back-action optical trapping of dielectric nanoparticles," *Nature Physics*, vol. 5, no. 12, pp. 915–919, 2009.

[47] K Okamoto and S Kawata, "Radiation force exerted on subwavelength particles near a nanoaperture," *Physical review letters*, vol. 83, no. 22, p. 4534, 1999.

[48] H. A. Bethe, "Theory of diffraction by small holes," *Physical review*, vol. 66, no. 7-8, p. 163, 1944.

[49] A. A. Al Balushi, A. Kotnala, S. Wheaton, R. M. Gelfand, Y. Rajashekara, and R. Gordon, "Label-free free-solution nanoaperture optical tweezers for single molecule protein studies," *Analyst*, vol. 140, no. 14, pp. 4760–4778, 2015.

[50] Y. Pang and R. Gordon, "Optical trapping of a single protein," *Nano Letters*, vol. 12, no. 1, pp. 402–406, 2012.

[51] J. Berthelot, S. S. Aćimović, M. L. Juan, M. P. Kreuzer, J. Renger, and R. Quidant, "Three-dimensional manipulation with scanning near-field optical nanotweezers," *Nature Nanotechnology*, vol. 9, no. 4, pp. 295–299, 2014.

[52] S. Kerman, C. Chen, Y. Li, W. Van Roy, L. Lagae, and P. Van Dorpe, "Raman fingerprinting of single dielectric nanoparticles in plasmonic nanopores," *Nanoscale*, vol. 7, no. 44, pp. 18 612–18 618, 2015.

[53] R. A. Jensen, I.-C. Huang, O. Chen, *et al.*, "Optical trapping and two-photon excitation of colloidal quantum dots using bowtie apertures," *ACS photonics*, vol. 3, no. 3, pp. 423–427, 2016.

[54] M. U. Raza, S. S. S. Peri, L.-C. Ma, S. M. Iqbal, and G. Alexandrakis, "Self-induced back action actuated nanopore electrophoresis (sane)," *Nanotechnology*, vol. 29, no. 43, p. 435 501, 2018.

[55] D. Yoo, K. L. Gurunatha, H.-K. Choi, *et al.*, "Low-power optical trapping of nanoparticles and proteins with resonant coaxial nanoaperture using 10 nm gap," *Nano Letters*, vol. 18, no. 6, pp. 3637–3642, 2018.

[56] A. Kotnala, P. S. Kollipara, J. Li, and Y. Zheng, "Overcoming diffusion-limited trapping in nanoaperture tweezers using opto-thermal-induced flow," *Nano Letters*, vol. 20, no. 1, pp. 768–779, 2019.

[57] S. J. Yoon, D. I. Song, J. Lee, M.-K. Kim, Y.-H. Lee, and C.-K. Kim, "Hopping of single nanoparticles trapped in a plasmonic double-well potential," *Nanophotonics*, vol. 9, no. 16, pp. 4729–4735, 2020.

[58] Q. Jiang, B. Rogez, J.-B. Claude, G. Baffou, and J. Wenger, "Quantifying the role of the surfactant and the thermophoretic force in plasmonic nano-optical trapping," *Nano letters*, vol. 20, no. 12, pp. 8811–8817, 2020.

[59] D. G. Kotsifaki, V. G. Truong, and S. N. Chormaic, "Fano-resonant, asymmetric, metamaterial-assisted tweezers for single nanoparticle trapping," *Nano Letters*, vol. 20, no. 5, pp. 3388–3395, 2020.

[60] N. Li, J. Cadusch, A. Liu, A. J. Barlow, A. Roberts, and K. B. Crozier, "Algorithm-designed plasmonic nanotweezers: Quantitative comparison by theory, cathodoluminescence, and nanoparticle trapping," *Advanced Optical Materials*, vol. 9, no. 19, p. 2 100 758, 2021.

[61] W. Yang, M. van Dijk, C. Primavera, and C. Dekker, "Fib-milled plasmonic nanoapertures allow for long trapping times of individual proteins," *iScience*, vol. 24, no. 11, p. 103 237, 2021.

[62] C. Ying, E. Karakaci, E. Bermudez-Urena, *et al.*, "Watching single unmodified enzymes at work," *arXiv preprint arXiv:2107.06407*, 2021.

[63] B. Wu, Y. Lou, D. Wu, *et al.*, "Directivity-enhanced detection of a single nanoparticle using a plasmonic slot antenna," *Nano Letters*, vol. 22, no. 6, pp. 2374–2380, 2022.

[64] C. Hong and J. C. Ndukaife, "Scalable trapping of single nanosized extracellular vesicles using plasmonics," *arXiv preprint arXiv:2302.07370*, 2023.

[65] S. Duhr and D. Braun, "Why molecules move along a temperature gradient," *Proceedings of the National Academy of Sciences*, vol. 103, no. 52, pp. 19 678–19 682, 2006.

[66] Z. Xu, W. Song, and K. B. Crozier, "Direct particle tracking observation and brownian dynamics simulations of a single nanoparticle optically trapped by a plasmonic nanoaperture," *ACS Photonics*, vol. 5, no. 7, pp. 2850–2859, 2018.

[67] Q. Jiang, B. Rogez, J.-B. Claude, G. Baffou, and J. Wenger, "Temperature measurement in plasmonic nanoapertures used for optical trapping," *ACS Photonics*, vol. 6, no. 7, pp. 1763–1773, 2019.

[68] Q. Jiang, B. Rogez, J.-B. Claude, *et al.*, "Adhesion layer influence on controlling the local temperature in plasmonic gold nanoholes," *Nanoscale*, vol. 12, no. 4, pp. 2524–2531, 2020.

[69] D. V. Verschueren, S. Pud, X. Shi, L. De Angelis, L Kuipers, and C. Dekker, "Label-free optical detection of dna translocations through plasmonic nanopores," *ACS Nano*, vol. 13, no. 1, pp. 61–70, 2018.

[70] P. Rodríguez-Sevilla, Y. Zhang, P. Haro-González, *et al.*, "Thermal scanning at the cellular level by an optically trapped upconverting fluorescent particle," *Advanced Materials*, vol. 28, no. 12, pp. 2421–2426, 2016.

[71] P. Li, M. Jia, G. Liu, A. Zhang, Z. Sun, and Z. Fu, "Investigation on the fluorescence intensity ratio sensing thermometry based on nonthermally coupled levels," *ACS Applied Bio Materials*, vol. 2, no. 4, pp. 1732–1739, 2019.

[72] Y. Zhou, F. Qin, Y. Zheng, Z. Zhang, and W. Cao, "Fluorescence intensity ratio method for temperature sensing," *Optics Letters*, vol. 40, no. 19, pp. 4544–4547, 2015.

[73] R. Galvão, L. F. d. Santos, R. R. Gonçalves, and L. d. S. Menezes, "Fluorescence intensity ratio-based temperature sensor with single nd3+: Y2o3 nanoparticles: Experiment and theoretical modeling," *Nano Select*, vol. 2, no. 2, pp. 346–356, 2021.

[74] V. Kesarwani and V. K. Rai, "Fluorescence intensity ratio technique and its reliability," *Methods and Applications in Fluorescence*, vol. 10, no. 3, p. 034 006, 2022.

[75] K. Green, K. Huang, H. Pan, G. Han, and S. F. Lim, "Optical temperature sensing with infrared excited upconversion nanoparticles," *Frontiers in chemistry*, vol. 6, p. 416, 2018.

[76] S. A. Wade, S. F. Collins, and G. W. Baxter, "Fluorescence intensity ratio technique for optical fiber point temperature sensing," *Journal of Applied Physics*, vol. 94, no. 8, pp. 4743–4756, 2003.

[77] C. Wang, Y. Jin, R. Zhang, Q. Yao, and Y. Hu, "A review and outlook of ratiometric optical thermometer based on thermally coupled levels and non-thermally coupled levels," *Journal of Alloys and Compounds*, vol. 894, p. 162 494, 2022.

[78] E. N. Gerasimova, V. V. Yaroshenko, P. M. Talianov, *et al.*, "Real-time temperature monitoring of photoinduced cargo release inside living cells using hybrid capsules decorated with gold nanoparticles and fluorescent nanodiamonds," *ACS Applied Materials & Interfaces*, vol. 13, no. 31, pp. 36 737–36 746, 2021.

[79] L. H. Fischer, G. S. Harms, and O. S. Wolfbeis, "Upconverting nanoparticles for nanoscale thermometry," *Angewandte Chemie International Edition*, vol. 50, no. 20, pp. 4546–4551, 2011.

[80] F. Vetrone, R. Naccache, A. Zamarrón, *et al.*, "Temperature sensing using fluorescent nanothermometers," *ACS Nano*, vol. 4, no. 6, pp. 3254–3258, 2010.

[81] M. D. Eisaman, J. Fan, A. Migdall, and S. V. Polyakov, "Invited review article: Single-photon sources and detectors," *Review of scientific instruments*, vol. 82, no. 7, p. 071 101, 2011.

[82] M. Hennrich, T. Legero, A. Kuhn, and G. Rempe, "Photon statistics of a non-stationary periodically driven single-photon source," *New Journal of Physics*, vol. 6, no. 1, p. 86, 2004.

[83] M. Steiner, A. Hartschuh, R. Korlacki, and A. J. Meixner, "Highly efficient, tunable single photon source based on single molecules," *Applied physics letters*, vol. 90, no. 18, p. 183 122, 2007.

[84] P. Senellart, G. Solomon, and A. White, "High-performance semiconductor quantum-dot single-photon sources," *Nature nanotechnology*, vol. 12, no. 11, pp. 1026–1039, 2017.

[85] W Redjem, A Durand, T Herzig, *et al.*, "Single artificial atoms in silicon emitting at telecom wavelengths," *Nature Electronics*, vol. 3, no. 12, pp. 738–743, 2020.

[86] L. Novotny and B. Hecht, *Principles of nano-optics*. Cambridge university press, 2012.

[87] C. H. Bennett, G. Brassard, C. Crépeau, R. Jozsa, A. Peres, and W. K. Wootters, "Teleporting an unknown quantum state via dual classical and einstein-podolsky-rosen channels," *Physical review letters*, vol. 70, no. 13, p. 1895, 1993.

[88] Z. Sharifi, M. Dobinson, G. Hajisalem, A. Frencken, F. C. van Veggel, and R. Gordon, "Enhancing and isolating lanthanide-doped nanocrystals using double nanohole optical tweezers for quantum light sources at 1550 nm," in *2021 IEEE 16th Nanotechnology Materials and Devices Conference (NMDC)*, IEEE, 2021, pp. 1–4.

[89] P Siyushev, K Xia, R Reuter, *et al.*, "Coherent properties of single rare-earth spin qubits," *Nature Communications*, vol. 5, no. 1, p. 3895, 2014.

[90] T. Böttger, Y Sun, C. Thiel, and R. Cone, "Spectroscopy and dynamics of er 3+: Y 2 si o 5 at 1.5 μ m," *Physical Review B*, vol. 74, no. 7, p. 075 107, 2006.

[91] S Probst, H Rotzinger, A. Ustinov, and P. Bushev, "Microwave multimode memory with an erbium spin ensemble," *Physical Review B*, vol. 92, no. 1, p. 014 421, 2015.

[92] G. Liu and B. Jacquier, *Spectroscopic properties of rare earths in optical materials*. Springer Science & Business Media, 2006, vol. 83.

[93] B. Romeira and A. Fiore, "Purcell effect in the stimulated and spontaneous emission rates of nanoscale semiconductor lasers," *IEEE Journal of Quantum Electronics*, vol. 54, no. 2, pp. 1–12, 2018.

[94] S. A. Maier *et al.*, *Plasmonics: fundamentals and applications*. Springer, 2007, vol. 1.

[95] A. Teitelboim, B. Tian, D. J. Garfield, *et al.*, "Energy transfer networks within upconverting nanoparticles are complex systems with collective, robust, and history-dependent dynamics," *The Journal of Physical Chemistry C*, vol. 123, no. 4, pp. 2678–2689, 2019.

[96] B. Zhou, B. Shi, D. Jin, and X. Liu, "Controlling upconversion nanocrystals for emerging applications," *Nature nanotechnology*, vol. 10, no. 11, pp. 924–936, 2015.

[97] F. Wang, J. Wang, and X. Liu, "Direct evidence of a surface quenching effect on size-dependent luminescence of upconversion nanoparticles," *Angewandte Chemie International Edition*, vol. 49, no. 41, pp. 7456–7460, 2010.

[98] E. Desurvire and M. N. Zervas, "Erbium-doped fiber amplifiers: Principles and applications," *Physics Today*, vol. 48, no. 2, p. 56, 1995.

[99] D. Yuan, M. C. Tan, R. E. Riman, and G. M. Chow, "Comprehensive study on the size effects of the optical properties of nayf4: Yb, er nanocrystals," *The Journal of Physical Chemistry C*, vol. 117, no. 25, pp. 13 297–13 304, 2013.

[100] L. He, Ş. K. Özdemir, and L. Yang, "Whispering gallery microcavity lasers," *Laser & Photonics Reviews*, vol. 7, no. 1, pp. 60–82, 2013.

[101] B. C. Dave and S. B. Lockwood, "Sol–gel method," *Encyclopedia of Nanotechnology*, pp. 2459–2470, 2012.

[102] J. D. Wright and N. A. Sommerdijk, *Sol-gel materials: chemistry and applications*. CRC press, 2018.

[103] M. A. Aegerter and M. Mennig, *Sol-gel technologies for glass producers and users*. Springer Science & Business Media, 2013.

[104] J. S. Wang, C. M. Wai, G. J. Brown, and S. D. Apt, "Insulating oxide film formation with acid catalyzed hydrolysis of alkoxide precursors in supercritical fluid carbon dioxide," *RSC Advances*, vol. 5, no. 91, pp. 74 753–74 763, 2015.

[105] A. McCormick, "Recent progress in the study of the kinetics of sol-gel sio2 synthesis reactions," *Sol-gel Processing And Applications*, pp. 3–16, 1994.

[106] K. J. Vahala, "Optical microcavities," *Nature*, vol. 424, no. 6950, pp. 839–846, 2003.

[107] M. L. Gorodetsky and V. S. Ilchenko, "Optical microsphere resonators: Optimal coupling to high-q whispering-gallery modes," *JOSA B*, vol. 16, no. 1, pp. 147–154, 1999.

[108] A. L. Ravindranath, M. S. Shariatdoust, S. Mathew, and R. Gordon, "Colloidal lithography double-nanohole optical trapping of nanoparticles and proteins," *Optics express*, vol. 27, no. 11, pp. 16 184–16 194, 2019.

[109] H. Wang, X. Yin, M. Xing, *et al.*, "Thermal effects of er3+/yb3+-doped nayf4 phosphor induced by 980/1510 nm laser diode irradiation," *Journal of the American Ceramic Society*, vol. 101, no. 2, pp. 865–873, 2018.

[110] J. F. Suyver, J. Grimm, M. Van Veen, D. Biner, K. Krämer, and H.-U. Güdel, "Upconversion spectroscopy and properties of nayf4 doped with er3+, tm3+ and/or yb3+," *Journal of Luminescence*, vol. 117, no. 1, pp. 1–12, 2006.

[111] Z. Li and Y. Zhang, "An efficient and user-friendly method for the synthesis of hexagonal-phase nayf4: Yb, er/tm nanocrystals with controllable shape and upconversion fluorescence," *Nanotechnology*, vol. 19, no. 34, p. 345 606, 2008.

[112] P. Klán, T. Solomek, C. G. Bochet, *et al.*, "Photoremovable protecting groups in chemistry and biology: Reaction mechanisms and efficacy," *Chemical Reviews*, vol. 113, no. 1, pp. 119–191, 2013.

[113] A. Alizadehkhaledi, A. L. Frencken, M. K. Dezfouli, S. Hughes, F. C. van Veggel, and R. Gordon, "Cascaded plasmon-enhanced emission from a single upconverting nanocrystal," *ACS Photonics*, vol. 6, no. 5, pp. 1125–1131, 2019.

[114] L. Yang, "Fabrication and characterization of microlasers by the sol-gel method," Ph.D. dissertation, California Institute of Technology, 2005.

[115] Y. Yu, D. Wu, Y. Lou, *et al.*, "Boosting trapping in dark mode and emission in bright mode using a quad-nanohole," *Advanced Optical Materials*, p. 2 202 924, 2023.

[116] E. H. Toodeshki, A. L. Frencken, F. C. van Veggel, and R. Gordon, "Thermometric analysis of nanoaperture-trapped erbium-containing nanocrystals," *ACS photonics*, vol. 11, no. 4, pp. 1390–1395, 2024.

[117] D. Lu, S. K. Cho, S. Ahn, L. Brun, C. J. Summers, and W. Park, "Plasmon enhancement mechanism for the upconversion processes in $nayf_4$: Yb^{3+}, er^{3+} nanoparticles: Maxwell versus forster," *ACS Nano*, vol. 8, no. 8, pp. 7780–7792, 2014.

[118] W. M. Abbott, S. Corbett, G. Cunningham, *et al.*, "Solid state dewetting of thin plasmonic films under focused cw-laser irradiation," *Acta Materialia*, vol. 145, pp. 210–219, 2018.

[119] Y. Hu, S. Li, and H. Bao, "First-principles based analysis of thermal transport in metallic nanostructures: Size effect and wiedemann-franz law," *Physical Review B*, vol. 103, no. 10, p. 104 301, 2021.

[120] R. Powell, C. Y. Ho, and P. E. Liley, *Thermal conductivity of selected materials*. US Department of Commerce, National Bureau of Standards Washington, DC, 1966, vol. 8.

[121] C. Stabler, A. Reitz, P. Stein, B. Albert, R. Riedel, and E. Ionescu, "Thermal properties of sioc glasses and glass ceramics at elevated temperatures," *Materials*, vol. 11, no. 2, p. 279, 2018.

[122] M. Assael, E Charitidou, C. N. de Castro, and W. Wakeham, "The thermal conductivity of n-hexane, n-heptane, and n-decane by the transient hot-wire method," *International Journal of Thermophysics*, vol. 8, pp. 663–670, 1987.

[123] H. Lamb, "Xiii. on electrical motions in a spherical conductor," *Philosophical Transactions of the Royal Society*, no. 174, pp. 519–549, 1883.

[124] B. Rogez, Z. Marmri, F. Thibaudau, and G. Baffou, "Thermoplasmonics of metal layers and nanoholes," *APL Photonics*, vol. 6, no. 10, p. 101 101, 2021.

[125] Y. Ren, Q. Chen, M. He, X. Zhang, H. Qi, and Y. Yan, "Plasmonic optical tweezers for particle manipulation: Principles, methods, and applications," *ACS Nano*, vol. 15, no. 4, pp. 6105–6128, 2021.

[126] L. Li, F. Qin, Y. Zhou, Y. Zheng, J. Miao, and Z. Zhang, "Three-energy-level-cascaded strategy for a more sensitive luminescence ratiometric thermometry," *Sensors and Actuators A-Physical*, vol. 304, p. 111 864, 2020.

[127] A. Ćirić, J. Aleksić, T. Barudžija, *et al.*, "Comparison of three ratiometric temperature readings from the er^{3+} upconversion emission," *Nanomaterials*, vol. 10, no. 4, p. 627, 2020.

[128] G. Chen and P. Hui, "Thermal conductivities of evaporated gold films on silicon and glass," *Applied Physics Letters*, vol. 74, no. 20, pp. 2942–2944, 1999.

[129] E. H. Toodeshki, A. L. Frencken, F. C. van Veggel, and R. Gordon, "Nanoscale upconverter thermometers in a double-nanohole optical tweezer," in *Optical Trapping and Optical Micromanipulation XX*, SPIE, vol. 12649, 2023, pp. 143–145.